

# Ambient Seismic Noise Tomography of Canada and Adjacent Regions:

## Part I Crustal Structures

Honn Kao<sup>1,2\*</sup>, Yannik Behr<sup>3,4</sup>, Claire Currie<sup>5</sup>, Roy Hyndman<sup>1,2</sup>, John Townend<sup>4</sup>, Fan-Chi Lin<sup>6</sup>,  
Michael H. Ritzwoller<sup>7</sup>, Shao-Ju Shan<sup>1</sup>, and Jiangheng He<sup>1</sup>

<sup>1</sup> Geological Survey of Canada, Pacific Geoscience Centre, Sidney, BC, Canada

<sup>2</sup> School of Earth and Ocean Sciences, University of Victoria, Victoria, BC, Canada

<sup>3</sup> Swiss Seismological Service, ETH Zurich, Switzerland

<sup>4</sup> Institute of Geophysics, Victoria University of Wellington, Wellington, New Zealand

<sup>5</sup> Department of Physics, University of Alberta, Edmonton, Alberta, Canada

<sup>6</sup> Division of Geological and Planetary Sciences, California Institute of Technology, Pasadena, CA,  
United States

<sup>7</sup> Department of Physics, University of Colorado at Boulder, Boulder, CO, United States

\* Corresponding Author, postal address: Geological Survey of Canada, Pacific Geoscience Centre,  
9860 West Saanich Road, Sidney, B.C. V8L 4B2, Canada; phone: 1-250-363-6625; email:  
hkao@nrcan.gc.ca

(submitted to *JGR-SE*, July 16, 2013)

23 **Abstract.** This paper presents the first continental-scale study of the crust and upper mantle shear-  
24 velocity ( $V_s$ ) structure of Canada and adjacent regions using ambient noise tomography. Continuous  
25 waveform data recorded between 2003 and 2009 with 788 broadband seismograph stations in Canada  
26 and adjacent regions are used in the analysis. The higher primary frequency band of the ambient noise  
27 provides better resolution of crustal structures than previous tomographic models based on earthquake  
28 waveforms. Prominent low-velocity anomalies are observed at shallow depths (<20 km) beneath the  
29 Gulf of St. Lawrence in east Canada, the sedimentary basins of west Canada, and the Cordillera. In  
30 contrast, the Canadian Shield exhibits high velocities. We characterize the crust–mantle transition in  
31 terms of not only its depth and velocity but also its sharpness, defined by the thickness of the transition  
32 and the amount of velocity increase. Considerable variations in the physical properties of the crust–  
33 mantle transition are observed across Canada. Positive correlations between the crustal thickness,  
34 Moho velocity, and the thickness of the transition are evident throughout most of the craton except near  
35 Hudson Bay where the uppermost mantle  $V_s$  is relatively low. Prominent vertical  $V_s$  gradients are  
36 observed in the mid-crust beneath the Cordillera and in the craton beneath most of the Canadian Shield.  
37 The mid-crust velocity contrast beneath the Cordillera may correspond to a detachment zone associated  
38 with high temperatures immediately beneath, whereas the large mid-crust velocity gradient beneath the  
39 Canadian Shield probably represents a rheological boundary between the upper and lower crust.

40

## 41 **1. Introduction**

42 The continental lithosphere of Canada contains a record of tectonic events that have shaped the  
43 region over the last 4 Gyr, from the ancient orogens that formed the cratonic core to on-going  
44 deformation of the more juvenile accreted terranes of the Canadian Cordillera. This area, which  
45 extends for >3000 km between the Atlantic and Pacific Oceans and a similar distance north–south  
46 (Figure 1), can be divided into three major geological domains: orogenic belts (the tectonically active

47 Cordillera in the west and the inactive Appalachian and Innuitian in the east and north, respectively);  
48 the central Archean shield; and the surrounding younger platforms (including sedimentary basins  
49 underlain by the Archean rocks) [e.g., *Fulton, 1989; Vincent, 1989; Wheeler et al., 1997*]. Present-day  
50 tectonic activity occurs mainly in the west in the Cordillera, where subduction of the Juan de Fuca and  
51 Explorer plates beneath the North America plate takes places in the south and strike-slip motion  
52 between North America and the Pacific plate takes place further north (Figure 1). The last tectonic  
53 events on the east Appalachian and arctic Innuitian regions were the Taconic orogeny in the Early  
54 Paleozoic and the Eurekan orogeny in the Early Paleocene, respectively [*Okulitch and Trettin, 1991;*  
55 *Williams, 1979*]. The tectonic history thus varies dramatically from west to east and there are associated  
56 significant variations in lithospheric structure as explored in this study.

57 Both global and regional tomographic studies using earthquake sources have identified the  
58 systematic seismic velocity differences between the continent's cratonic center and the Cordillera and  
59 Cascadia subduction zone in the west [*Dalton et al., 2009; Lebedev and van der Hilst, 2008; Lekic and*  
60 *Romanowicz, 2011; Mercier et al., 2009; Simmons et al., 2010; van der Lee and Frederiksen, 2005; and*  
61 *references therein*]. The lateral transition from high upper mantle velocities associated with the cold  
62 craton to lower velocities beneath the hot Cordillera is abrupt [e.g., *Hyndman and Lewis, 1999*], but  
63 geographically complex [e.g., *Bank et al., 2000; Bensen et al., 2008; Frederiksen et al., 1998; Mercier*  
64 *et al., 2009; van der Lee and Frederiksen, 2005*]. Similarly, variations in crustal thickness across the  
65 continent have been extensively documented, with average to thick (40–45 km) crust in the craton and  
66 other stable areas in the middle of the continent [e.g., *Cook et al., 2010; Ma et al., 2012; Mooney et al.,*  
67 *1998; Perry et al., 2002*] and thin (~35 km) crust beneath the Cordillera [*Clowes et al., 2005; Mooney*  
68 *et al., 1998; Perry et al., 2002*]. There have been numerous studies addressing aspects of the seismic  
69 and thermal structures of various parts of the Canadian Shield [e.g., *Audet and Mareschal, 2004; Cheng*  
70 *et al., 2002; Frederiksen et al., 2007; Guillou-Frottier et al., 1996; Mareschal et al., 2005; Perry et al.,*

71 2006; *Shapiro et al.*, 2004b; and references therein] and the Cordillera [e.g., *Cassidy*, 1995;  
72 *Frederiksen et al.*, 1998; *Hyndman et al.*, 2005; *Mercier et al.*, 2009]. However, a detailed  
73 understanding of exactly how the transition in seismic velocity and crustal thickness from craton to  
74 Cordillera is accommodated requires a consistent and systematic approach spanning the entire region.

75 Ambient seismic noise tomography has recently become a well-established velocity mapping  
76 technique [e.g., *Behr et al.*, 2011; *Bensen et al.*, 2009; *Fulton*, 1989; *Ritzwoller et al.*, 2011; *Sabra et*  
77 *al.*, 2005; *Shapiro et al.*, 2005; *Tibuleac et al.*, 2011; *Wapenaar et al.*, 2008]. One of its advantages over  
78 traditional earthquake-based tomographic methods is its avoidance of heterogeneously distributed  
79 earthquake sources. Also, due to the high-frequency spectral content of the ambient noise used, this  
80 technique is particularly well suited to high-resolution imaging of velocity structures at crustal and  
81 uppermost mantle depths [*Behr et al.*, 2011; *Lin et al.*, 2008; *Lin et al.*, 2007]. Its recent widespread  
82 adoption has been promoted by the rapid expansion of global, regional, and local broadband  
83 seismograph networks. Efficient seismic data management and distribution, as well as increasing  
84 computational capacity, have also only recently made possible the processing of the large volumes of  
85 ambient seismic noise data involved.

86 By utilizing ambient noise records made throughout Canada and adjacent parts of the United States  
87 and Greenland (Figure 2), the goal of this study is to establish the crust and upper mantle velocity  
88 structure at a resolution as high as the local and regional data permit and to investigate all the  
89 geological provinces with the same methodology and processing procedures. Based on the surface  
90 wave tomographic results obtained, we then estimate the 3D shear-velocity ( $V_s$ ) distributions to upper  
91 mantle depths. We focus mainly on crustal and uppermost mantle structures with special emphasis on  
92 the topography and character of the Moho discontinuity. Finally, we address how abruptly the crustal  
93 velocity and thickness vary among the geological provinces and discuss the tectonic implications of  
94 these variations.

95

## 96 **2. Data and Analysis**

97 In this section, we first describe the ambient noise data used in our analysis, followed by an  
98 introduction to the data processing procedures, tomographic inversion, and the conversion of surface  
99 wave results obtained at different periods to 3D shear-wave velocities.

### 100 **2.1. Ambient Seismic Noise Data**

101 Continuous digital broadband seismic waveforms recorded by the Canadian National Seismograph  
102 Network (CNSN) and the Portable Observatories for Lithospheric Analysis and Research Investigating  
103 Seismicity (POLARIS) between 2003 and 2009 constitute the core component of our data set. To  
104 provide velocity resolution near the boundaries of the main study area, we also make use of broadband  
105 waveforms from stations north of 40°N within the United States, mainly from the United States  
106 Advanced National Seismic System and the dense temporary United States Transportable Array  
107 (USArray), east of 150°W in Alaska (mainly the Alaska Regional Seismic Network), and along the  
108 western coastline of Greenland (included as part of the Global Seismic Network). We further include  
109 stations of the Canadian High Arctic Seismic Monitoring Experiment (CHAME) to provide critical  
110 data coverage for the arctic north. Figure 2 shows the station distribution of our dataset and the  
111 corresponding ray path coverage.

112 CNSN, POLARIS and CHAME waveform archives were obtained from the CNSN Data Center,  
113 whereas the other data were obtained from the Data Management Center of the Incorporated Research  
114 Institutions for Seismology (IRIS). The combined dataset includes records from 843 stations covering a  
115 time window of 2557 days. Because not all stations operated at the same time, especially those of the  
116 USArray, it is not possible to have a complete combination of all station pairs for any given day. On  
117 average, our dataset has half to two thirds of the stations represented on any one day.

### 118 **2.2. Seismic Waveform Processing**

119 We follow the procedures outlined by *Bensen et al.* [2007] to process the waveform data. For each  
120 station, the vertical component waveforms are first split into one-day segments, followed by the  
121 subtraction of the amplitude mean and trend, removal of the instrument response, time-domain  
122 normalization using the running-absolute-mean method, and spectral whitening. Cross correlation  
123 functions (CCFs) are calculated for the daily waveforms for each station pair. We employ a two-stage  
124 stacking scheme, first monthly then total, to accommodate the large volume of data. On average, each  
125 station yields more than 12,000 monthly CCFs. For some long-running stations, the number of CCFs  
126 exceeds 25,000.

127 Figure 3 shows four representative examples from CNSN stations with the final stacked CCF.  
128 Because of the large number of samples, we plot only the trace with the highest signal-to-noise (S/N)  
129 ratio for each 100 km distance interval. For the two stations on the east and west coasts (LMN and  
130 PGC, respectively; Figures 3a and b), the Rayleigh wave move-out can be clearly observed across the  
131 continent to offsets of more than 5000 km. For the stations located in the northwest (INK) and  
132 southeast (ACTO), the move-out spans more than 4000 km (Figures 3c and d). All four stations show  
133 pronounced differences between the causal (positive) and acausal (negative) branches of the CCF,  
134 which are most likely due to azimuthally biased noise source distributions [e.g., *Stehly et al.*, 2006].

### 135 **2.3. Dispersion Measurement**

136 The positive and negative branches of the correlation function are averaged to give the symmetric  
137 component, which is used thereafter to estimate the Rayleigh wave dispersion curves [*Bensen et al.*,  
138 2007]. The commonly used frequency–time analysis (FTAN) with phase-matched filtering [*Levshin*  
139 *and Ritzwoller*, 2001] is applied to track the dispersion ridge from the spectral image and to minimize  
140 the effects of spurious noise glitches or jumps in group arrival times. The corresponding phase  
141 velocities are obtained using the approach described by *Lin et al.* [2008].

142 For each station pair, we conduct the phase-matched filtering FTAN for the period range of 5–250 s.

143 If the analysis results in no output, due to the abrupt discontinuity in the dispersion measurements, we  
144 incrementally decrease the maximum period (from 250 s to 200, 150, 100, 75, or 50 s) to maintain both  
145 the quantity and quality of our input data.

146 In Figure 4, we show the stacked symmetric CCFs and the corresponding dispersion curves for two  
147 representative station pairs spanning the western (PGC–FFC, station distance 1625 km) and eastern  
148 (DRLN–FFC, station distance 3064 km) halves of the Canadian continent, respectively (station  
149 locations shown in Figure 2). The dispersive characteristics of Rayleigh waves can be clearly  
150 recognized on traces derived from stacking only one year of ambient noise data (top traces, Figure 4).  
151 As the duration of the data used in the stacking increases from one to three years, the S/N ratios  
152 improve accordingly (middle traces, Figure 4). However, the S/N improvement becomes much less  
153 significant when we increase the stacking dataset from three to seven years (bottom traces, Figure 4),  
154 suggesting that the benefit of including data beyond 2009 is probably limited for present purposes.

155 As our dataset covers all the northern states of the US in which ambient noise tomography has been  
156 undertaken previously [*Bensen et al.*, 2008; *Bensen et al.*, 2009; *Shen et al.*, 2013], it is important to  
157 ensure that the stacked CCFs and dispersion measurements derived in this study are consistent with  
158 those reported from earlier studies. For this purpose, we compare our results with the stacked CCFs  
159 available from the Data Management Center of IRIS (IRIS DMS Product, Western US Ambient Noise  
160 Cross-Correlations, by Mikhail Barmine and Michael Ritzwoller, published electronically June 2012,  
161 Incorporated Research Institutions for Seismology, Last accessed March 26, 2013,  
162 <http://www.iris.edu/dms/products/ancc-ciei>). A representative example is shown in Figure 5 (RLMT  
163 and NLWA; locations shown in Figure 2). Although the datasets used in the two studies span different  
164 years, all the waveform characteristics in the stacked CCF are remarkably similar. The dispersion  
165 measurements are essentially identical except at the longest periods (>90 s) where the difference is  
166 about 0.2 km/s due to the deterioration of data resolution. This provides us with confidence in both the

167 dataset and analysis employed in this study.

## 168 **2.4. Surface Wave Tomography Inversion**

169 We use the method of *Barmin et al.* [2001] to derive tomographic images from Rayleigh wave  
170 dispersion data. For each period, the inversion estimates the 2D distribution of group and phase  
171 velocity perturbations across a spherical grid of  $1^\circ$  spacing in a damped least-squares sense. The  
172 damping is controlled by two parameters specifying the weight of smoothing and the width of the  
173 smoothing area. We take an empirical approach to determine the optimal combination of the two  
174 weighting parameters, by systematically examining the mean and standard deviation of the overall  
175 misfit function of the inversion. The parameters corresponding to the least damping with a mean misfit  
176 close to zero and a small standard deviation are adopted in deriving our final velocity results which is  
177 shown in Figure 6. A more detailed discussion of our tomographic inversion results will be given in the  
178 next section.

179 Several previous studies have argued that the tomographic resolution inferred from the commonly  
180 used checkerboard test may be misleading [e.g., *Leveque et al.*, 1993] or difficult to interpret [e.g.,  
181 *Simons et al.*, 2002]. In this study, we choose the spike-perturbation test, as outlined by *Barmin et al.*  
182 [2001], to assess the resolution of our results. Specifically, we place a spike-like perturbation at a given  
183 node of the inversion grid and then examine the corresponding inversion output. The spatial resolution  
184 at that node is defined by the minimum distance at which a neighboring spike can be unambiguously  
185 identified. As expected, we find that the spatial resolution is closely linked to the density of local  
186 stations and the number of ray paths.

## 187 **2.5. Conversion From Surface Wave Tomography to 3D Grid Tomography**

188 To convert the set of surface wave maps at successive periods into a 3D shear-velocity model, we  
189 employ the method of *Shapiro et al.* [2004a] as implemented by *Behr et al.* [2010; 2011]. At each  $1^\circ$   
190 grid point, a new dispersion curve is computed by interpolating between the values at successive



191 periods. Each newly derived dispersion curve is then inverted for a 1D shear-velocity profile using the  
192 Neighbourhood Algorithm (NA) [Sambridge, 1999a; Sambridge, 1999b], resulting in 4949 shear  
193 velocity–depth profiles. The NA is a direct search method, similar to the Monte-Carlo algorithm or  
194 simulated annealing, which solves optimization problems by exploring the range of possible solutions  
195 in a quasi-random manner. It returns best-fitting models and an estimate of the distribution of models in  
196 the parameter space as a function of their misfit. For each 1D shear-velocity model, the misfit is  
197 computed as the least-squares difference between the dispersion curve of the model and the one  
198 constructed from the surface-wave maps. This approach enables us to evaluate the resolution and the  
199 level of ambiguity of each best-fitting shear-velocity model. We employ the software package Dinver  
200 ([www.geopsy.org](http://www.geopsy.org)) [Wathelet, 2008] which combines the forward modeling algorithm of *Dunkin* [1965]  
201 with an improved version of the original NA. The current version of the Dinver algorithm does not  
202 allow for parameterization of a top water layer, and therefore areas of shallow waters (e.g., lakes or  
203 bays) are given a top layer of extremely low shear strength. Inversions for areas with a thick water  
204 column, such as the Pacific and Atlantic oceans, are disregarded in our analysis.

205 One hundred new models and their misfits are computed for each of the 300 NA iterations, resulting  
206 in 30,000 shear-velocity models being evaluated at each grid point. We follow the scheme of  
207 CRUST2.0 to parameterize the crustal portion of each model as a stack of five homogeneous, isotropic  
208 layers corresponding to sediments, sedimentary basement, upper crust, middle crust and lower crust.  
209 One or two mantle layers are setup to extend the model to upper mantle depths. We assume that the  
210 shear modulus is independent of frequency (i.e., shear  $Q$  is essentially infinite). This significantly  
211 simplified the forward calculation and can be justified on the ground that our study focus is the crust  
212 where the  $Q$  tends to be larger than that in the mantle. Another justification is that much of the region  
213 of study is stable craton with large  $Q$  values. Although the top layer of sediments may have relatively  
214 low  $Q$ , its effect is generally negligible in our case due to its thin thickness (0 to a few km).

215 Each layer is characterized by thickness, compressional velocity ( $V_p$ ), shear velocity ( $V_s$ ) and  
216 density. The NA varies the thickness,  $V_p$  and  $V_s$  but not density for each layer at each iteration and  
217 computes the misfit. Density has been shown to have only minor influence on the resulting dispersion  
218 curve [Wathelet, 2005] and has therefore been kept constant at the values of CRUST2.0 in the crust and  
219 PREM in the mantle.

220 To obtain a stable (reproducible) result, it is necessary to impose some constraints on the parameter  
221 space. We achieve this by incorporating *a priori* knowledge of the shear-velocity profile at a particular  
222 grid point. For the crust, we allow the NA to vary each inverted parameter by 20% around the  
223 CRUST2.0 model [Bassin *et al.*, 2000]. The crustal thickness is taken from the LITH5.0 model [Perry  
224 *et al.*, 2002], where available, and from CRUST2.0 otherwise. Values for the mantle layers are taken  
225 from the PREM model [Dziewonski and Anderson, 1981] and we again allow the parameters to vary by  
226 20%.

227 We conduct forward modeling to estimate the uncertainty in the inversion results. For each best-  
228 fitting model, we systematically perturb each inverted parameter and calculate the root-mean-square  
229 (RMS) error between observed and synthetic dispersion curves. Because the overall fit to the phase  
230 velocity dispersion curve is 2–3 times better than the fit to the group velocity [Lin *et al.*, 2008], we  
231 adjust the relative weighting between the two by a factor of 2.5 to prevent the uncertainty estimate  
232 being dominated by the group velocity misfit. The parameter's range of uncertainty is set at the values  
233 corresponding to a 5% RMS increase.

234 At each grid point, we calculate the weighted average of the top 5% best-fitting model samples  
235 using the inverse of the misfit value as the weighting factor. These weighted best-fitting 1D models are  
236 then combined and linearly interpolated laterally to form the final pseudo-3D model. The weighted  
237 average approach is a practical and perhaps better alternative to choosing the best-fitting model,  
238 especially when multiple model samples have almost the same misfit values.

239 In Figure 7, we show representative examples of the NA inversion results for points in four different  
240 tectonic settings: the Cordillera, the Interior Platform, the Canadian Shield, and the Appalachian (see  
241 Figures 1 and 9c for locations). The surface-wave dispersion curves are clearly different from one node  
242 to another. One important feature in the group velocity dispersion curves is the broad trough in the 15–  
243 30 s period range that effectively constrains the depth of the crust–mantle transition [Lebedev *et al.*,  
244 2013]. The trough is the narrowest and shifted toward shorter periods in the Cordillera, where the  
245 Moho is relatively shallow (Figure 7a). A broader trough is observed inside the craton where the crust  
246 is thicker (Figures 7b and c). In comparison, the broadness of the trough is intermediate in the  
247 Appalachian where the Moho depth is in between those of the Cordillera and the craton (Figure 7d).

248 The robustness of the inversions is well illustrated by the concentration of best-fitting models in a  
249 relatively narrow portion of the model space (Figure 7). For nearly all the NA inversions that we have  
250 performed, the results are robust and can be reproduced with different sets of starting models. Figure 8  
251 shows the distribution of best-model misfits. Overall, better results are obtained for the Canadian  
252 Shield and the Appalachian regions (misfit  $<0.07$  km/s) than for the Cordillera and the Interior Platform  
253 ( $<0.15$  km/s).

254

### 255 **3. Seismic Inversion Results**

256 In this section, we first present the surface-wave tomography results and then the pseudo-3D shear-  
257 velocity results computed from ambient seismic noise CCFs. We emphasize the variation of crustal  
258 structures, including the depth and velocity characteristics of the Moho. The dominant frequencies of  
259 ambient seismic noise are well suited to study such depths, in contrast to those of most earthquake  
260 tomographic studies that focus on lower frequencies and correspondingly greater depths.

#### 261 **3.1. Surface Wave Tomography–General Features**

262 Since the vertical component waveforms are used in our ambient seismic noise analysis, our surface

263 wave tomography corresponds to the distribution of group and phase velocities of Rayleigh waves. In  
264 Figure 6, we show the velocity distributions, horizontal resolution, and depth sensitivity for three  
265 periods (10, 35, and 50 s), which are most sensitive to the depth ranges of 5–15 km, 15–50 km, and 30–  
266 80 km, respectively. The horizontal resolution corresponds to one standard deviation of the best-fitting  
267 Gaussian surface at each point [Lin *et al.*, 2007].

268 In general, group and phase velocity distributions are similar at all periods. At shorter periods (e.g.,  
269 10 s, Figure 6a), velocity anomalies are dominated by large-scale sedimentary basins and upper crust  
270 structures. Prominent low-velocity anomalies are observed for the Gulf of St. Lawrence Basin in the  
271 east, the sedimentary basins of west Canada, and in the Cordillera. In contrast, the Canadian Shield  
272 exhibits high velocities.

273 The low-velocity signature beneath the Gulf of St. Lawrence disappears at periods larger than 35 s.  
274 Similarly, the low-velocity anomalies associated with the Cordillera are much less visible. Overall, the  
275 velocity contrast between high and low anomalies is smaller, and the high velocities associated with the  
276 craton expand slightly toward the west under the western Canadian sedimentary basin (i.e., the Interior  
277 Platform (Figures 1 and 6b). Such a westward expansion of the high-velocity anomaly is even more  
278 prominent at longer periods (e.g., 50 s, Figure 6c).

279 Generally speaking, our data provide reasonable constraints on Rayleigh-wave velocities to latitudes  
280 of  $\sim 70^\circ\text{N}$ . Further north, the station distribution becomes sparse and the image resolution deteriorates.  
281 Taking the 10 s period as an example, the large volume of data results in a horizontal resolution of 150  
282 km or less for most grid points south of  $70^\circ\text{N}$ . The spatial resolution also deteriorates with increasing  
283 period as the number of useful CCFs decreases. The image deterioration becomes progressively worse  
284 for the northern region.

### 285 **3.2. Pseudo-3D Grid Tomography**

286 We invert for the shear-velocity ( $V_s$ ) distribution across the study region at  $1^\circ$  intervals. In Figure 9,

287 we show the pseudo-3D tomographic images at three depths corresponding to the top sedimentary layer  
288 and upper crust (5 km), the lower crust (25 km), and the uppermost mantle (50 km). E–W and N–S  
289 vertical cross sections are shown in Figure 10.

290 At the 5 km depth, there are a number of prominent low- $V_s$  anomalies. The most pronounced are on  
291 the western side of the continent, including the Cascadia forearc (the Georgia-Pudget-Wallamette basin  
292 of southwestern British Columbia, western Washington, and central-western Oregon), the Rocky  
293 Mountains (eastern Idaho, western Montana and Wyoming), and the Canadian Cordillera (Figures 1  
294 and 9). The low- $V_s$  anomalies in the northern US have been documented previously using the same  
295 tomography technique [Bensen *et al.*, 2009; Shen *et al.*, 2013]. The low- $V_s$  signature of the Cordillera  
296 and Cascadia forearc remains visible down to the uppermost mantle. This is particularly evident when  
297 comparing the profile through the Canadian Cordillera to the one through the western Canadian Shield  
298 (Profiles 1–1' vs. 2–2', Figure 10). We also find that the shallow low velocities beneath the Cordillera  
299 extend north to the Yukon and Northwest territories (Figure 9).

300 For east Canada, the  $V_s$  patterns are similar between the western and the eastern parts of the  
301 Canadian Shield, as shown by Profiles 2–2' and 3–3' in Figure 10, respectively. The most obvious  
302 shallow low- $V_s$  anomaly is located beneath the southern Gulf of St. Lawrence sedimentary basin.  
303 Another low- $V_s$  anomaly is found beneath Lake Superior where an ancient mid-continental rift system  
304 is inferred from geological and geophysical data [Cannon *et al.*, 1989]. However, there is no evidence  
305 of thick sediments because the rift system went through a stage of tectonic inversion 1.1 b.y. ago with  
306 the central graben being uplifted by at least 5 km [Cannon *et al.*, 1989]. Consequently, we suspect that  
307 the observed low- $V_s$  anomaly beneath Lake Superior is not a manifestation of a thick sedimentary  
308 basin. Instead, it might be an artifact due to the leaking effect from the top water layer.

309 From the three E–W profiles (A–A', B–B', and C–C' in Figure 10), it is clear that the highest  $V_s$  at  
310 the uppermost mantle depths is not directly associated with the center of the Canadian Shield. Instead,

311 the highest  $V_s$  corresponds to the stable Interior Platform and the outer rim of the Canadian Shield  
312 (900–1400 km in Profile A–A', 650–2050 km in Profile B–B', and 1000–2500 and 3250–3900 km in  
313 Profile C–C'). In general, the inner part of the Shield appears to have  $V_s$  consistently lower than that of  
314 the outer rim for all of the mantle depths resolvable by our data.

315 There are two interesting features in Profile C–C' that are distinct from the other profiles. One is the  
316 dome-like high- $V_s$  anomaly in the mid- and lower crust between ~20 and 40-km depths just to the west  
317 of Profile 2–2' (the region centered at the US-Canada border between Montana and Manitoba, Figure  
318 9b). The other is the generally broader vertical transition between lower crust and uppermost mantle, a  
319 feature we discuss in some detail in the next section.

### 320 **3.3. Crust–mantle Transition**

321 The crust–mantle transition (“Moho”) was first discovered in Europe as a subsurface velocity  
322 interface across which  $V_p$  rapidly increases from ~5.6 to >7.75 km/s and  $V_s$  from 3.27 to 4.18 km/s  
323 [*Mohorovicic*, 1910]. Early studies concluded that the Moho generally corresponded to the depth at  
324 which the density of earth materials increases dramatically due to either compositional or phase  
325 changes [e.g., *Adams and Williamson*, 1923; *Green and Ringwood*, 1972; *Ito and Kennedy*, 1971].  
326 However, as refraction seismology was undertaken in different part of the world, geophysicists realized  
327 that substantial variations exist in the Moho discontinuity's depth distribution, the magnitude of the  
328 velocity contrast, and its vertical dimension [e.g., *Cook et al.*, 2010; *Mooney*, 1987]. Furthermore,  
329 different remote sensing techniques (seismic refraction, seismic reflection, magnetotelluric  
330 measurements, etc.) often yield different Moho depths that may correspond to different physical  
331 aspects of the crust–mantle transition [e.g., *Catchings and Mooney*, 1991; *Cook et al.*, 2010; *Mooney*  
332 *and Brocher*, 1987]. Consequently, an appropriate modifier is usually placed in front of the term  
333 “Moho” (such as refraction Moho, reflection Moho, or electric Moho) to indicate the specific  
334 geophysical technique employed in the survey [e.g., *Cook et al.*, 2010].

335 Globally, the Moho discontinuity is recognized as a large velocity increase from  $V_p \sim 6.8\text{--}7.3$  km/s to  
 336  $V_p \sim 8.2$  km/s [e.g., *Mooney et al.*, 1998]. Using a typical  $V_p\text{--}V_s$  relationship derived from laboratory  
 337 data [*Christensen*, 1996], the corresponding  $V_s$  jump is estimated to be 0.42–0.82 km/s (from  $V_s$  of  
 338 3.73–4.13 to 4.55 km/s). In Figure 10, we mark the two depths at which the  $V_s$  has increased from a  
 339 typical crustal velocity to a typical upper mantle velocity by 50% and 85% with the blue and red lines,  
 340 respectively. The schematic diagram in Figure 11 illustrates how these two depths are determined.  
 341 Specifically for each grid point, we first identify the lower crust shear velocity ( $V_{s,crust}$ ) and the  
 342 uppermost mantle velocity ( $V_{s,mantle}$ ) from the corresponding  $V_s$  profile. The  $V_s$  increased at a given  
 343 level is defined as

$$344 \quad V_r = V_{s,crust} + r (V_{s,crust} - V_{s,mantle}) \quad (1)$$

345 where  $r$  is the percentage of  $V_s$  increase (e.g., 50% or 85%).

346 In Figure 12, the depth range corresponding to this 50%–85%  $V_s$  increase, hereafter referred to as  
 347  $dZ_{50\%-85\%}$ , is colored in gray. Most of the large velocity gradients occur where  $V_s$  jumps from  $\leq 3.8$  km/s  
 348 to  $\geq 4.2$  km/s (Figure 10). However, there are exceptions where the downward velocity increase is  
 349 gradual rather than abrupt. Given the varying thickness of the velocity increase from crust to uppermost  
 350 mantle, the depth of a specific  $V_s$  or an abrupt velocity jump (which is the common definition of a  
 351 “refraction Moho,” [e.g., *Steinhart*, 1967]) cannot fully characterize the crust–mantle transition.  
 352 Similarly, the reflection Moho and electric Moho, which have been defined as “the deepest, high-  
 353 amplitude, laterally extensive reflection or group of reflections” and “a step change in electrical  
 354 conductivity” present in the vicinity of the corresponding refraction Moho, respectively [e.g., *Cook et*  
 355 *al.*, 2010; *Jones and Ferguson*, 2001; *Klemperer et al.*, 1986], cannot well serve the purpose in some  
 356 areas either.

357 The appropriate definition of the “Moho” depends on the application. While the ambient seismic  
 358 noise dispersion measurement is not the ideal tool to pinpoint the location of a seismic reflector such as

359 the Moho, it is capable of distinguishing a sharp velocity discontinuity from a gradual one. This unique  
360 advantage enables us to examine the crust–mantle transition from a different perspective. For places  
361 where the  $V_s$  increase is gradual, a gradational transition between crustal and mantle compositions is  
362 implied. It is not yet possible to determine whether the gradational layer is an intercalated mixture of  
363 crustal and mantle rocks or another mixed structure.

364 As a general measure appropriate for many applications, including isostasy calculations, we propose  
365 a more comprehensive method of characterizing the crust–mantle transition. In Figure 13, the depth  
366 contours corresponding to  $V_s$  increase 50% and 85% from lower crust to uppermost mantle are plotted  
367 along with the corresponding velocities,  $V_{50\%}$  and  $V_{85\%}$ , and their differences. Although it is convenient  
368 to identify the depth contour of  $V_{85\%}$  (i.e.,  $Z_{85\%}$ ) as a proxy for the "ambient noise" Moho, it is  
369 important to realize that the abruptness of the crust–mantle transition is clearly not uniform across the  
370 continent. Most areas beneath which a relatively sharp Moho discontinuity, i.e.,  $dZ_{50\%-85\%} < 2$  km, is  
371 inferred beneath the Canadian Shield (Figure 13c). For other regions, using a single Moho depth to  
372 define the crust–mantle transition is probably inappropriate.

373 To first order, the depth distribution of the 85% crust–mantle  $V_s$  increase (i.e.,  $Z_{85\%}$ , Figure 13a) is  
374 similar to that presented by *Bensen et al.* [2009] and *Cook et al.* [2010] for regions south and north of  
375 the Canada–US border, respectively. Relatively thick crust is found surrounding the Canadian Shield,  
376 whereas thin crust is associated with active deformation such as the Cordillera and Cascadia. Overall,  
377 the crustal thickness beneath most of the Canadian craton is in the range of 35–41 km.

378 The Moho  $V_s$ , as represented by  $V_{50\%}$  and  $V_{85\%}$ , shows a clear difference between the Cordillera and  
379 the continental interior (Figures 13d and 13e). Relatively low  $V_{85\%}$  (i.e.,  $\leq 4.1$  km/s) is observed beneath  
380 the entire western orogenic belt including the Canadian Cordillera, the Columbia Plateau, and the  
381 Cascadia forearc. In contrast, most of the Canadian craton and central US (e.g., northern Central  
382 Lowlands and Great Plains) are associated with relatively high Moho  $V_s$ . One exception is the central



383 Hudson Bay Platform where the corresponding  $V_{85\%}$  is obviously lower. The relatively low crustal  
384 velocity beneath the Hudson Bay was also documented in a previous study using a regional dataset of  
385 ambient seismic noise [Pawlak *et al.*, 2010].

386 For the cratonic region, an overall correlation amongst crustal thickness, Moho  $V_s$ , and the thickness  
387 of the crust–mantle transition can be recognized (Figure 13). As the crust thickens from the center of  
388 the Canadian Shield outward, the corresponding  $V_{85\%}$  and  $dZ_{50\%-85\%}$  increase as well, except near  
389 Hudson Bay where the  $V_{85\%}$  appears to be the lowest. Such correlation does not seem to hold for the  
390 Cordillera, either. While the Cordillera has a thinner crust and a lower  $V_{85\%}$  than the craton, the  
391 thickness of the crust–mantle transition is in the middle range varying between 2 and 5 km.

### 392 **3.4. Large Velocity Gradients in Mid-Crust**

393 Our tomographic results show the existence of large vertical  $V_s$  gradients within the mid-crust in  
394 some areas. Examples of these large mid-crust gradients can be recognized from the six cross sections  
395 across different parts of the continent in Figure 10 and the  $V_s$  profiles shown in Figure 14. Their  
396 geographic distribution, however, is not uniform across Canada, and their depth distribution varies  
397 from one region to another. In most cases, the  $V_s$  increase is between 0.2 and 0.5 km/s.

398 The most prominent mid-crust  $V_s$  gradient is observed beneath the Cordillera, best shown in the  
399 Profile 1–1' of Figure 10. Its depth appears to increase to the south. The section just south of Profile A–  
400 A' has a large mid-crust  $V_s$  gradient at ~5 km depth. It is located at ~9 and 11 km beneath the sections  
401 around the Profile B–B' and to the south of C–C', respectively. In addition, the large mid-crust  $V_s$   
402 gradient is not continuous across the entire Cordillera. Several gaps, each a few hundreds of km long,  
403 exist between sections where the large mid-crust  $V_s$  gradient is clear.

404 Another region in which a prominent mid-crust  $V_s$  gradient is observed is the craton beneath part of  
405 the Canadian Shield. The western half of the Superior Province (between 2300 and 3100 km in the  
406 Profile C–C', Figure 10; also the profiles GL-A and GL-C, Figure 14) shows a clear  $V_s$  jump at the

407 depth of ~12 km. This large  $V_s$  jump defines the lower boundary of the upper crust.

408 A large mid-crust  $V_s$  gradient also exists beneath the easternmost section of Profile B–B' where the  
409 Canadian Shield meets the Appalachian belt (Figure 10). However, it is not common in the  
410 Appalachians because similar  $V_s$  jumps are not observed beneath the easternmost end of the Profile C–  
411 C'. Unfortunately, limited data resolution prevents us from obtaining a high-resolution velocity image  
412 for this part of the continent. Future investigation with a denser regional seismograph network in the  
413 region is needed.

414

#### 415 **4. Quantitative Comparison with Previous Models**

416 In this section, we make quantitative comparisons of our results with previous models in the  
417 literature that were derived from different datasets. By systematically examining and characterizing  
418 both the similarity and difference, the purpose is to provide an objective assessment of our model in  
419 terms of regional variation and data resolution.

##### 420 **4.1. Lithoprobe Transects**

421 In Figure 14, we show ten selected  $V_s$  profiles from our results and compare them with nearby  
422 seismic reflection profiles from the Lithoprobe program [*Clowes et al.*, 1984; *Cook*, 2002]. The map  
423 locations of the ten  $V_s$  profiles are marked in Figure 9c as red crosses. These examples are chosen  
424 because either they show a gradual crust–mantle transition or the location of the largest velocity  
425 gradient is inconsistent with the previously reported Moho depths. Specifically, we compare five  $V_s$   
426 profiles in the vicinity of Profile B–B' with Lithoprobe transects AB-CAT1 (at a distance of ~1200 km;  
427 Figure 10), THOT-S1a (~1500 km), WS-2a (~2300 km), WS-1a (~2600 km), and another five  $V_s$   
428 profiles in the vicinity of Profile C–C' with transects GL-C (~2400 km) and GL-A (~2700 km).

429 The base of common deep crustal sub-horizontal reflectivity usually is close to the defined Moho  
430 but there are some exceptions. For the transect AB-CAT1 passing through the Interior Platform in

431 central Alberta, the bottom part of the zone containing strong seismic reflectors was used in previous  
432 studies to define the “reflection” Moho at a depth of 40 km [Perry *et al.*, 2002]. In our results, it  
433 corresponds to a velocity increase over a 7-km range between 33 km and 40 km ( $V_s$  profiles at 54°N,  
434 115°W and 53°N, 115°W, Figure 14). Similar situations are observed for transect THOT-S1a through  
435 the Western Canadian Sedimentary Basin (55°N, 107°W) and transect WS-2a through the western part  
436 of the Superior Craton (50°N, 95°W), except that the Moho discontinuity in the LITH5.0 model is ~4  
437 km deeper. Near the northern end of transect WS-1a in the central Superior Craton (52°N, 90°W), the  
438 discrepancy among our  $V_s$  profile, the seismic reflection image, and the LITH5.0 model is apparent as  
439 the bottom of the strong seismic reflector zone (i.e., the reflection Moho) is located between the largest  
440 velocity gradient at 32–38 km and the Moho depth in the LITH5.0 model (i.e., the refraction Moho) at  
441 43 km.

442 One of the biggest inconsistencies between the crust–mantle velocity gradients found in our analysis  
443 and the Moho depths in the LITH5.0 model is observed in the vicinity of Lake Superior, where  
444 transects GL-A and GL-C are located. Taking transect GL-C as an example, the  $V_s$  profile near the  
445 northwestern end (48°N, 91°W) show a large velocity gradient between 36 and 41 km near the bottom  
446 of the zone of strong seismic reflectors. In comparison, the Moho depth is reported at 49 km in the  
447 LITH5.0 model, below which another gradual  $V_s$  increase is observed. Similarly, the  $V_s$  profile near the  
448 southeastern end of the transect GL-C (47°N, 89°W) exhibits a big velocity jump at 38–43 km that  
449 approximately coincides with the bottom of the strong seismic reflectors (Figure 14). A much smaller  
450 velocity increase is found at ~54 km depth where the LITH5.0 model defines the Moho discontinuity,  
451 although evidence from the seismic reflection image is unclear.

452 For the three locations near transect GL-A that passes through the center of Lake Superior (49°N,  
453 87°W; 48°N, 87°W; 46°N, 88°W), the largest velocity gradients all correspond to strong seismic  
454 reflectors within rather than at the bottom of the reflector zones. Our  $V_s$  profiles show that the velocity

455 begins to increase gradually at the depths where strong seismic reflectors become apparent, and the  
456 increase extends down to the bottom of the reflector zone where the Moho depth is defined in the  
457 LITH5.0 model.

#### 458 **4.2. “Ambient Noise” Moho vs. “Reflection” and “Refraction” Moho**

459 In a global review of seismic reflection/refraction studies of the continental lithosphere, *Mooney and*  
460 *Brocher* [1987] pointed out that the lower crust appears to consist of laminated high- and low-velocity  
461 layers with typical thicknesses of 100–200 m, making it much more reflective than either the upper  
462 crust or the uppermost mantle. Therefore, the Moho depth determined from seismic reflection data may  
463 involve a clear reflector, but often is defined as the bottom of the reflective layers that generally  
464 coincides with the refraction Moho to within a few kilometers. For places with complex lower crustal  
465 and/or uppermost mantle structures, however, constructive and destructive interferences among seismic  
466 signals from different structures may lead to ambiguous interpretations of the Moho depths [e.g.,  
467 *Catchings and Mooney*, 1991; *Cook*, 2002]. The occasionally significant discrepancies are well  
468 documented in the results of the Lithoprobe project in which the refraction and reflection Moho depths  
469 can differ by as much as 10 km [*Cook et al.*, 2010].

470 While the reflection and refraction Mohos are determined from  $V_p$  and P-wave impedance contrast,  
471 the "ambient-noise" Moho is based on the  $V_s$  distribution. Shear and compressional wave interface  
472 depths are expected to be similar but there is a possibility of differences. A direct comparison between  
473 the “ambient-noise” Moho relief determined in this study (Figures 12 and 13) and the Moho relief  
474 inferred from Lithoprobe reflection and refraction data (Figures 2 and 3 of *Cook et al.* [2010]) suggests  
475 that all three tend to agree that thin and thick crust is located beneath the Cordillera and craton,  
476 respectively. However, for a large portion of the cratonic region, the refraction Moho usually is the  
477 deepest, followed by the reflection Moho, and the ambient-noise Moho usually is the shallowest. The  
478 difference is generally <5 km. When a significant discrepancy exists between the reflection and

479 refraction Moho, we notice that the ambient-noise Moho tends to be more consistent with the one that  
480 is better constrained. For example, the local variation in the ambient-noise Moho depth beneath central-  
481 northern Alberta (Figures 13a and 13b) is visible on the refraction Moho, as constrained by several  
482 Lithoprobe refraction transects, but not clear on the reflection Moho [Cook *et al.*, 2010]. Similarly, the  
483 locally shallower ambient-noise Moho beneath the Ontario–Quebec border is more consistent with the  
484 reflection Moho with constraints from a number of reflection profiles but not with the refraction Moho.

485 There are exceptions where the three Moho depths do not necessarily follow the downward order of  
486 ambient-noise, reflection, then refraction. One such example is observed in central Quebec (e.g., 53°N,  
487 74°W) where the ambient-noise Moho is the shallowest ( $Z_{50\%}$  and  $Z_{85\%}$  at 32 and 36 km, respectively,  
488 Figure 13) followed by the refraction Moho (~39 km) and the reflection Moho (~45 km). Another  
489 similar example is in southern Quebec near the Canada–US border (e.g., 45°N, 73°W). Once again, the  
490 ambient-noise Moho is the shallowest ( $Z_{50\%}$  and  $Z_{85\%}$  at 35 and 38 km, respectively), followed by the  
491 refraction Moho at ~42 km and the reflection Moho at ~45 km. Notice that the numbers of available  
492 Lithoprobe transects, refraction or reflection, for both regions are very few, meaning that the inferred  
493 reflection or refraction Moho depths are less constrained.

494 It will need more detailed local studies to thoroughly investigate the relationships among different  
495 Moho depths and their physical relevance to the crust–mantle transition. In this paper, we provide only  
496 an initial discussion on this subject. In theory, different approaches are sensitive to different aspects of  
497 the velocity structure. While seismic reflection is best at illuminating velocity interfaces with large  
498 impedance contrast, seismic refraction is generally sensitive to the variation of velocity at depth. The  
499 difference may result in the refraction Moho being systematically deeper than the reflection Moho,  
500 especially if the bottom of the lower crust is not strongly reflective [Catchings and Mooney, 1991].  
501 Since we define the ambient-noise Moho based on the sharpness of  $V_s$  variation across the crust–mantle  
502 transition, our result is expected to be more sensitive to the overall composition change than just the

503 impedance contrast or the velocity of the bottom layer of the lower crust.

504 A recent study on the physical properties of the Paleozoic Cabo Ortegal Complex of NW Spain  
505 suggests that the crust–mantle transition is a gradation from felsic gneisses to ultramafic rocks with  
506 eclogites and mafic granulites in between [Brown *et al.*, 2009]. In such a scenario, the velocity Moho  
507 (reflection or refraction) actually corresponds to the boundary between the gneisses and the eclogite at  
508 a shallower depth, whereas the petrological Moho is located between the mafic granulites and  
509 ultramafic peridotites at a deeper depth. The fact that the ambient-noise Moho is often located  
510 shallower than the reflection or refraction Moho seems to imply that the deepest structure of the crust–  
511 mantle transition does not necessarily correspond to the largest velocity jump. It may be that the top of  
512 our Moho gradient layer marks the beginning of the gneisses–eclogite transition and the base represents  
513 the downward transition to ultramafic peridotite.

#### 514 **4.3. Previous Crustal and Tomography Models**

515 Given the large number of previous studies of the seismic velocity structures of North America, it is  
516 impractical to compare our results with all the models described in the literature. There are also  
517 important issues to be considered before a meaningful comparison can be conducted, including the  
518 availability of model parameters, the scale and geographic coverage of each model, and the model  
519 resolution. However, to facilitate quantitative comparison of our model with any model of readers'  
520 interest, we have compiled a digital version of Figure 13 listing the physical parameters of the inferred  
521 “ambient noise” Moho and an ASCII table showing our tomography results (available online as  
522 electronic supplements). For demonstration purposes, we conduct comparisons with two crustal models  
523 cited frequently in this paper, CRUST2.0 [Bassin *et al.*, 2000] and LITH5.0 [Perry *et al.*, 2002], and  
524 two recent North American tomography models, NA04 [van der Lee and Frederiksen, 2005] and NA07  
525 [Bedle and van der Lee, 2009], that are available in digital form at the IRIS website.

526 In Figure 12, we plot the Moho depths of the LITH5.0 [Perry *et al.*, 2002] and CRUST2.0 [Bassin *et*

527 *al.*, 2000] models as dashed blue and red lines, respectively, to summarize previous observations.

528 Depending on the percentage of  $V_s$  increase defined in equation (1), the average depth difference

529 between our model and the two previous crustal models may vary from -4.4 km ( $Z_{50\%}$  - *CRUST2.0*) to

530 6.5 km ( $Z_{100\%}$  - *LITH5.0*), as shown by the histograms in Figure 15.

531 Taking the  $Z_{85\%}$  as a proxy for the "ambient noise" Moho, our result is on average 0.6 km shallower

532 than that of *CRUST2.0* model. This difference is negligible given the model uncertainty in our

533 inversion. The corresponding standard deviation is 5.8 km. With respect to the *LITH5.0* model, our

534 model is on average 0.9 km deeper with a slightly larger standard deviation of 6.2 km. We notice that

535 much of the high standard deviations stems from nodes where the discrepancy between the *CRUST2.0*

536 and *LITH5.0* models exceeds 10 km. In other words, we will inevitably encounter a large discrepancy

537 with respect to one or other of the two models at these nodes. We list the corresponding Moho depths

538 of the *CRUST2.0* and *LITH5.0* models in the electronic supplement for the convenience of readers

539 interested in comparing specific nodes/regions.

540 Both *NA04* and *NA07* models provide seismic velocity distribution for the entire upper mantle from

541 70 km to 670 km at interval of 20 km, whereas our tomography results only have adequate resolution

542 for shallow depths (<100 km). Therefore, only the top two layers of the *NA04* and *NA07* models (i.e.,

543 70 km and 90 km) are used in the comparison.

544 At a depth of 70 km, our model is on average 0.21 and 0.24 km/s slower than *NA04* and *NA07*

545 models, respectively (Figure 16). The corresponding standard deviation of the velocity difference is

546 0.16 km/s for both. Most of the nodes with large discrepancies (i.e., larger than one standard deviation)

547 are located near the boundary of our model where the ray path coverage is not optimal. However, there

548 are places where the difference is large and yet the resolution length is reasonable (e.g., central Canada

549 north of  $\sim 60^\circ\text{N}$ ). Further investigation of these places using an independent dataset and/or

550 methodology should be planned.

551 Similarly, for the 90 km depth, the average  $V_s$  of our model is 0.14 and 0.17 km/s slower than that of  
552 NA04 and NA07 models, respectively (Figure 16). The standard deviation stays almost unchanged  
553 (0.17 for NA04 and 0.16 for NA07), and many of the nodes with  $V_s$  differences exceeding one standard  
554 deviation are the same ones as identified at the 70-km depth. This suggests that the difference between  
555 our tomography model and those derived from earthquake data is probably systematic and strongly  
556 data dependent.

557

## 558 **5. Implications and Discussion**

559 Shear velocity is one of the fundamental physical properties characteristic of earth materials. It is  
560 strongly linked to composition and state such as temperature and in turn to the patterns of present  
561 deformation and evolutionary history of tectonic/geological structures. 3D velocity tomography is  
562 especially useful in delineating deep structures and assessing their tectonic implications. Although a  
563 comprehensive discussion of the various tectonic implications of our ambient seismic noise  
564 tomography is both important and desirable, it is impractical to include everything in this article. We  
565 therefore limit the discussion to topics directly relevant to our data and seismological results. Other  
566 important subjects for which our data provide new constraints, such as the temperature variations in the  
567 lithosphere across different tectonic/geologic provinces and the density distribution within the crust and  
568 uppermost mantle, require additional analysis and will be covered in a subsequent article.

### 569 **5.1. Surface Geology and Topography of the Crust–mantle Transition**

570 In general, the surface geology of Canada (south of 70°N) can be divided into five components,  
571 namely, the Cascadia forearc, the North America Cordillera, the sedimentary basins overlying the  
572 craton (i.e., the Interior Platform and the Hudson Bay Platform), the exposed craton (i.e., the Canadian  
573 Shield), and the Appalachian orogen [e.g., *Wheeler et al.*, 1997]. Previous crustal models have  
574 indicated that the Cascadia forearc and Cordillera are associated with relatively thin (~35 km and less)



575 crust, whereas the crustal thickness in the stable craton region is 40–45 km [Bassin *et al.*, 2000;  
576 Mooney *et al.*, 1998; Perry *et al.*, 2002]. The significant differences in the average elevation and Moho  
577 depth have been explained as the thermal isostasy buoyancy effect due to higher lithospheric  
578 temperatures in the Cordillera [e.g., Currie and Hyndman, 2006; Hyndman and Currie, 2011].

579 While the average crustal thickness inferred from our tomography results is in good agreement with  
580 previous models, we notice that the Moho relief within each geological region, as manifest by the depth  
581 contours of 50% and 85%  $V_s$  increase from crust to uppermost mantle, is not as uniform as previously  
582 mapped (Figures 10–14). For example, the Moho depth beneath the Cordillera shows local variations  
583 that fluctuate between 25 and 38 km (e.g., Profile 1–1', Figure 12). Locations with particularly shallow  
584 crust–mantle transition generally coincide with known volcanic areas where the crustal structure is  
585 dominated by the corresponding volcanic processes. Presumably the Moho topography is also related  
586 to the mechanical strength/rigidity profile of the lithosphere, and may be controlled by the pattern of  
587 mantle flow beneath [Currie and Hyndman, 2006]. Although it is beyond the scope of this study to  
588 determine the exact physics implied by the Moho topography, our results suggest that the nature of the  
589 dominant process must involve factors that vary locally (i.e., on scales of 100–1000 km).

590 Even within the cratonic region east of the Cordillera, regional variations in the crustal thickness are  
591 observed (Figures 12 and 13). While the general trend of the Moho depth is to increase gradually from  
592 north to south, there are clear local highs and lows along the E–W direction (Profiles A–A', B–B', and  
593 C–C' in Figure 12, and Figures 13a and 13b). It is important to point out that previous studies on the  
594 effective elastic thickness of the lithosphere also show significant variations for different parts of the  
595 craton [e.g., Burov *et al.*, 1998; Flück *et al.*, 2003; Hyndman *et al.*, 2009; Mareschal *et al.*, 2005; Wu,  
596 1991]. Such variations have been attributed to the strong lateral variations in the thermal regime of the  
597 lithosphere [Flück *et al.*, 2003; Hyndman *et al.*, 2009; Wang and Mareschal, 1999], large-scale crustal  
598 heterogeneity [Burov *et al.*, 1998; Guillou-Frottier *et al.*, 1996], or both [Mareschal *et al.*, 2005; Wu,

599 1991]. Our results suggest that the lateral variation of crustal structures, including the thickness, may  
600 also play a role in controlling the effective elastic thickness of the lithosphere.

## 601 **5.2. Sharpness of the Crust–mantle Transition**

602 The sharpness of a velocity interface can be characterized by two parameters: its thickness and the  
603 amount of velocity change. Given the same amount of velocity change, a sharp interface means that it  
604 is very thin with a large velocity jump whereas a diffused one spans a finite depth range with a gradual  
605 velocity variation. Most previous studies using global crustal models, however, have not adequately  
606 addressed the sharpness of the crust–mantle transition. Our results provide systematic estimates of the  
607 thickness and corresponding  $V_s$  increase of the crust–mantle transition for most of the North American  
608 continent north of 40°N that, in turn, would constrain interpretations of the formation and subsequent  
609 tectonic evolution of the continental crust.

610 It is interesting to point out that there seems to be a slight anti-correlation between the crust–mantle  
611 transition thickness  $dZ_{50\%-85\%}$  and the amount of velocity change  $dV_{50\%-85\%}$  (Figures 13c and 13f).  
612 Overall, the Canadian Shield is associated with a relatively smaller  $dZ_{50\%-85\%}$  and a larger  $dV_{50\%-85\%}$ . As  
613 the  $dZ_{50\%-85\%}$  increases from the Canadian Shield outward, the corresponding  $dV_{50\%-85\%}$  decreases  
614 accordingly but the relationship is obviously not linear. One clear exception is the American mid-west  
615 region between 90°W and 100°W where both the  $dZ_{50\%-85\%}$  and  $dV_{50\%-85\%}$  are large.

616 It has been suggested that the structural details associated with the crust–mantle transition may be  
617 too complex and varied to prevent a single, universally applicable interpretation of the continental  
618 Moho discontinuity [Cook *et al.*, 2010]. In fact, a comprehensive compilation of “geophysical” Moho  
619 distribution from Lithoprobe data has concluded that the continental Moho discontinuity is not a simple  
620 boundary and may not always coincide with the petrological Moho [e.g., Cook *et al.*, 2010; Moores,  
621 1982], although a large portion of Canada remains unexplored by Lithoprobe-type transects. Our  
622 ambient noise tomography results confirm that the crust–mantle transition is characterized by a finite

623 zone whose thickness and velocity contrast may vary from one geological/tectonic region to another.

624       Nonetheless, if we take the seismic velocity as a reasonable proxy for the density and composition  
625 of crustal materials [*Christensen and Mooney, 1995*], then the sharpness of the ambient-noise Moho  
626 can be viewed as a first-order indicator of how much the position, geometry, and physical properties of  
627 the crust–mantle transition have been altered over the geological history. Further studies with high  
628 resolution at local and regional scales are obviously needed to better understand the geological and  
629 tectonic significance of the variation in the sharpness of the ambient-noise Moho.

### 630 **5.3. Tectonic Significance of the Large Mid-Crust Velocity Gradients**

631       The discovery of a common mid-crust velocity discontinuity, often called the Conrad discontinuity,  
632 was based on seismic signals refracted from a velocity interface located at a depth of 15–20 km with  $V_p$   
633 of ~6.5 km/s [*Richter, 1958*]. Although it was originally interpreted to be the boundary between a  
634 granitic upper crust and a basaltic lower crust, later research indicated that such a simple interpretation  
635 could not explain the observed complexity [e.g., *Fountain and Christensen, 1989*]. Not only is the mid-  
636 crust discontinuity far less frequently observed than the Moho, but the corresponding seismic velocities  
637 are often not those of typical granitic or basaltic compositions [*Christensen and Mooney, 1995*].

638       One recent explanation for a mid-crustal boundary was provided by *Mazzotti and Hyndman [2002]*  
639 based on the distribution of regional seismicity, heat flow measurements, geodetic data, and numerical  
640 modeling of the northern Cordillera region. They proposed that the lower crust is very weak due to  
641 consistently high temperatures beneath the Cordillera. According to that model, a mid-crustal  
642 detachment zone is formed above the weakest point and facilitates the northeastward movement of the  
643 quasi-rigid upper crust overthrusting the craton. We speculate that the large mid-crust velocity  
644 gradients observed beneath the Cordillera, as described in Section 3.4, are also related to such mid-  
645 crustal detachment zones. The mid-crust velocity contrast in this region probably represents a  
646 thermodynamically controlled interface that may have played an important role in the regional thick-

647 skinned tectonics.

648 For the large mid-crust velocity gradient beneath part of the Canadian Shield (Figures 10, 13, and  
 649 14), the most straightforward interpretation would be a rheological boundary between the upper and  
 650 lower crust formed at earlier times when temperatures were much higher. The corresponding velocity  
 651 difference may be explained by a change of composition from an average mix of 45% granitic gneiss  
 652 and 5% amphibolite at the upper crust depths to 15% granitic gneiss and 35% amphibolite in the lower  
 653 crust [Christensen and Mooney, 1995]. Depending on other possible factors such as the depth of the  
 654 discontinuity and its sharpness, the exact compositional ratio may vary from one place to another.

#### 655 **5.4. Possible Effect of Anisotropy**

656 The velocity structures derived from our tomography inversion are assumed isotropic. This  
 657 assumption is obviously too simplistic for places where azimuthal anisotropy has been demonstrated  
 658 previously, such as in Cascadia [Currie *et al.*, 2004; Eakin *et al.*, 2010; Rieger and Park, 2010], the  
 659 Superior province [Darbyshire *et al.*, 2007], and the Appalachians [Barruol *et al.*, 1997; Levin *et al.*,  
 660 1999]. Based on earthquake data, Yuan and Romanowicz [2010] estimate the amount of azimuthal  
 661 anisotropy in the upper mantle beneath the North America craton to be of the order of 1%.

662 In a recent global earthquake surface wave dispersion study, Nettles and Dziewonski [2008] pointed  
 663 out that the transverse component of shear velocity (i.e.,  $V_{SH}$ ) is on average 2–6% faster than the radial  
 664 component ( $V_{SV}$ ) at the uppermost mantle depths beneath Canada. Using the dense US Transportable  
 665 Array ambient noise data, Moschetti *et al.* [2010b] concluded that the mean amplitude of radial  
 666 anisotropy in the lower crust and upper mantle beneath the western US are 3.6% and 5.3%,  
 667 respectively. Because both NA04 and NA07 models are derived from inversion of shear and Rayleigh  
 668 waveforms of moderate-magnitude ( $M_s \geq \sim 5$ ) regional earthquakes located around the periphery of the  
 669 North America continent, the reported  $V_s$  values presumably represent the isotropic  $V_s$ , which is  
 670 approximately the mean of  $V_{SH}$  and  $V_{SV}$ . In contrast, the  $V_s$  values determined in our study are in fact

671  $V_{SV}$  because our dataset contains only Rayleigh waves. Therefore, a 2–6% radial anisotropy at the  
672 uppermost mantle would yield a velocity reduction of 0.05–0.14 km/s between our results and the two  
673 previous models. This estimate appears to be somewhat smaller than that shown in Figure 16. Further  
674 studies to characterize the amount and distribution of both azimuthal and radial anisotropy beneath  
675 Canada are needed.

## 676 **5.5. Future Efforts**

677 Although the dataset used in constructing NA07 has considerably more ray paths due to additional  
678 earthquake sources and the deployment of the temporary US Transportable Array, the data coverage for  
679 Canada is still not ideal. Nonetheless, a big advantage of earthquake data is that the seismic energy can  
680 penetrate to great depths, and thus earthquake tomography is often capable of resolving deep structures.  
681 In contrast, ambient seismic noise tomography does not require well-distributed earthquake sources but  
682 the data generally do not have sufficient low-frequency energy to resolve velocity anomalies at depth.

683 One possible effort is to take a hybrid approach to integrate the data constraints from both  
684 earthquake and ambient noise sources. We have experimented with this approach by incorporating a  
685 small set of earthquake dispersion curves [*Darbyshire, 2005; Darbyshire et al., 2007*] into our analysis,  
686 but with limited success. Taking the phase velocity measurements for the station pair of ATGO and  
687 ATKO for example, the dispersion curve derived from ambient seismic noise has good S/N in the 3–23  
688 s period range, whereas the dispersion curve from earthquake data spans 24–186 s. However, there is a  
689 sudden 0.1 km/s jump between the upper end of the ambient-noise dispersion curve and the lower end  
690 of the earthquake one.

691 We suspect the jump as an artifact arising from the different processing procedures and controlling  
692 parameters employed in different studies (e.g., the assumed number of cycles between station pairs).  
693 Several recent efforts of joint interpretation of ambient seismic noise and earthquake dispersion data  
694 also observed a discrepancy between earthquake and ambient noise dispersion curves, although the

695 disagreement was smaller and diminished as more earthquake measurements are added to the dataset  
696 [e.g., *Moschetti et al.*, 2010a; *Shen et al.*, 2013; *Zhou et al.*, 2012]. In other words, it might not be  
697 appropriate to simply combine dispersion measurements found in the literature with the seismic  
698 ambient noise dispersion curves to form a hybrid dataset. A systematic and uniform re-processing of an  
699 expanded dataset is probably necessary to ensure their internal consistency.

700 A logical next step to better resolve the crustal thickness and velocity structures of our model is to  
701 combine constraints from dispersion data and other types of measurements that are more sensitive to  
702 velocity contrast at depths. This can be achieved, for example, by jointly inverting receiver functions  
703 with dispersion curves, as demonstrated by the recent study of *Shen et al.* [2013] for the central and  
704 western US. A similar effort for Canada is planned in the near future.

705 Finally, our results can provide important constraints on the density distribution within the crust.  
706 Given the relatively flat surface topography throughout most of the cratonic region, the observed relief  
707 of the crust–mantle transition cannot be interpreted as an Airy isostatic effect. Furthermore, an overall  
708 correlation between a relatively thick crust (>40 km) and a relatively high Moho  $V_s$  ( $\geq 4.25$  km/s) can  
709 be established for the cratonic region (Figure 13). Such correlation could be qualitatively explained in  
710 terms of local density variations according to the linear velocity–density relationship determined from  
711 laboratory data for continental crustal materials [*Christensen and Mooney*, 1995]. However, a  
712 quantitative approach to determine the density and temperature distributions from our tomography  
713 model is not straightforward: that analysis is the focus of a forthcoming paper [*Currie et al.*, 2013,  
714 manuscript in preparation].

715

## 716 **6. Conclusions**

717 The long geological evolution of Canada has involved many tectonic processes operating over an  
718 area of 10 million km<sup>2</sup> and a timespan of 4 Gyr. This paper presents the first continental-scale study of

719 the shear-velocity structure of Canada and the adjacent region using ambient noise tomography,  
720 providing better resolution and more homogeneous coverage than previous tomographic studies based  
721 on earthquake waveforms.

722 The vertical component of continuous waveform data between 2003 and 2009 from 788 broadband  
723 seismograph stations in Canada and adjacent regions are collected and processed following the  
724 procedures described in *Bensen et al.* [2007]. Stacked cross correlation functions of all station pairs are  
725 analyzed with a phase-matching filter to obtain both the group and phase-velocity dispersion curves of  
726 the Rayleigh wave. The dispersion measurements for regions overlapping with previous studies are  
727 consistent with published results and our results indicate that improvement in the signal-to-noise ratio  
728 of the stacked waveforms becomes marginal once the amount of data exceeds 3 years.

729 Surface-wave tomography inversion is carried out from the dispersion data to estimate the phase and  
730 group velocity distribution at  $1^\circ$  interval for periods between 5 and 100 s. In general, the patterns of  
731 group and phase velocity distributions are similar to each other at all periods. At shorter periods (e.g.,  
732 10 s), prominent low-velocity anomalies are observed in the Gulf of St. Lawrence in the east, the  
733 sedimentary basins of west Canada and the Cordillera. In contrast, the Canadian Shield exhibits high  
734 velocities. The velocity contrast between high and low anomalies becomes smaller at longer periods  
735 (e.g.,  $\geq 35$  s), and the high velocities associated with the craton appear to expand slightly toward the  
736 west under the western Canadian sedimentary basin.

737 For each grid point, a 1D shear-velocity ( $V_s$ ) profile is inverted from the dispersion data using the  
738 Neighbourhood Algorithm [*Sambridge, 1999a; Sambridge, 1999b*]. The resulted 4949  $V_s$  profiles are  
739 then combined into a pseudo-3D  $V_s$  model that extends down to  $\sim 100$ -km depth. Overall, the inner part  
740 of the Canadian Shield has  $V_s$  consistently lower than that of the outer rim throughout the mantle  
741 depths resolvable by our data.

742 To better characterize the nature of crust–mantle transition, we propose that both the thickness and

743 the amount of velocity increase should be included in addition to the depth and velocity of the Moho  
744 discontinuity. In this study, the "ambient noise" Moho is defined as the depth where the  $V_s$  increase is  
745 85% from the typical value in the lower crust to uppermost mantle ( $Z_{85\%}$  and  $V_{85\%}$  in Figure 13). Such  
746 defined Moho is slightly different from other types (e.g., reflection Moho, refraction Moho, or electric  
747 Moho), but the difference is generally less than 5 km. The thickness of crust–mantle transition is  
748 defined as the depth difference between places where the crust–mantle  $V_s$  increase is 50% and 85% (the  
749  $dZ_{50\%-85\%}$  in Figure 13). We have observed considerable variations in the depth,  $V_s$ , and sharpness of the  
750 crust–mantle transition across Canada. For the cratonic region, an overall correlation among the crustal  
751 thickness, Moho  $V_s$ , and the thickness of the transition can be recognized except in the Hudson Bay  
752 area where the Moho  $V_s$  is relatively low. Such correlation does not seem to hold for the Canadian  
753 Cordillera, either, where a modestly sharp transition is associated with thin crust and low Moho  $V_s$ .

754 Prominent mid-crust  $V_s$  gradient is observed beneath the Cordillera and in the craton beneath part of  
755 the Canadian Shield. While the mid-crust velocity contrast beneath the Cordillera may be related to a  
756 detachment zone due to the consistently high temperature beneath, the large mid-crust velocity gradient  
757 beneath the Canadian Shield could be interpreted as a rheological boundary between the upper and  
758 lower crust with an average mix of 45% granitic gneiss and 5% amphibolite in the upper crust and 15%  
759 granitic gneiss and 35% amphibolite in the lower crust.

760 Quantitative comparison of our tomography results with previous earthquake-based tomography  
761 models reveals that the  $V_s$  derived from ambient seismic noise is slightly lower (by  $\sim 0.2$  km/s at the 70  
762 and 90-km depths). This is likely caused by the effect of radial anisotropy in the uppermost. An attempt  
763 to build a hybrid dataset containing dispersion measurements from both ambient noise and earthquakes  
764 was not successful because the measurements are internally inconsistent. A systematic and uniform re-  
765 processing of an expanded dataset is probably necessary for this approach to work. Other research  
766 efforts in our plan include extending the current study to Love waves, characterizing the amount and



767 distribution of both azimuthal and radial anisotropy beneath Canada, and estimating the density and  
768 temperature distributions from our tomography model.

769

## 770 **Acknowledgment**

771 Fiona Darbyshire kindly provides the dispersion measurements of earthquake surface waves. Digital  
772 waveform data are obtained from the data centers of the Canadian Hazard Information Service and  
773 Incorporated Research Institutions for Seismology. We benefit from discussion with David Schneider,  
774 Sonya Dehler, and Yu-Lien Yeh. YB and JT acknowledge the support of the Marsden Fund of the Royal  
775 Society of New Zealand. MHR acknowledges support from US NSF grant EAR-1252085. This  
776 research is partially supported by a NSERC grant to HK (RGPIN 418268-2013). ESS contribution  
777 number XXXXXX.

778

779 **Electronic Supplement 1:** An ASCII file listing our tomography inversion results.

780 **Electronic Supplement 2:** An ASCII file listing physical parameters of the ambient-noise Moho  
781 determined in this study.

782

## 783 **References**

784 Adams, L. H., and E. D. Williamson (1923), Density distribution of the Earth, *Journal of the*  
785 *Washington Academy of Sciences*, 13, 413-428.

786 Audet, P., and J. C. Mareschal (2004), Variations in elastic thickness in the Canadian Shield, *Earth*  
787 *Planet. Sci. Lett.*, 226, 17-31, doi: 10.1016/j.epsl.2004.1007.1035.

788 Bank, C.-G., M. G. Bostock, R. M. Ellis, and J. F. Cassidy (2000), A reconnaissance teleseismic study  
789 of the upper mantle and transition zone beneath the Archean Slave craton in NW Canada,  
790 *Tectonophysics*, 319(3), 151-166, doi:110.1016/S0040-1951(1000)00034-00032.

- 791 Barmin, M. P., M. H. Ritzwoller, and A. L. Levshin (2001), A fast and reliable method for surface wave  
792 tomography, *Pure Appl. Geophys.*, *158*, 1351-1375.
- 793 Barruol, G., P. G. Silver, and A. Vauchez (1997), Seismic anisotropy in the eastern United States: Deep  
794 structure of a complex continental plate, *J. Geophys. Res.*, *102*, 8329–8348.
- 795 Bassin, C., G. Laske, and G. Masters (2000), The current limits of resolution for surface wave  
796 tomography in North America, *EOS Trans AGU*, *81*, F897.
- 797 Bedle, H., and S. van der Lee (2009), S velocity variations beneath North America, *J. Geophys. Res.*,  
798 *114*(B7), B07308, doi:07310.01029/02008JB005949.
- 799 Behr, Y., J. Townend, S. Bannister, and M. K. Savage (2010), Shear-velocity structure of the Northland  
800 Peninsula, New Zealand, inferred from ambient noise correlations, *J. Geophys. Res.*, doi:  
801 10.1029/2009JB006737.
- 802 Behr, Y., J. Townend, S. Bannister, and M. K. Savage (2011), Crustal shear wave tomography of the  
803 Taupo Volcanic Zone, New Zealand, via ambient noise correlation between multiple three-  
804 component networks, *Geochem. Geophys. Geosy.*, *12*, Q03015, doi:03010.01029/02010GC003385.
- 805 Bensen, G. D., M. H. Ritzwoller, and N. M. Shapiro (2008), Broadband ambient noise surface wave  
806 tomography across the United States, *J. Geophys. Res.*, *113*, B05306,  
807 doi:05310.01029/02007JB005248.
- 808 Bensen, G. D., M. H. Ritzwoller, and Y. Yang (2009), A 3-D shear velocity model of the crust and  
809 uppermost mantle beneath the United States from ambient seismic noise, *Geophys. J. Int.*, *177*(3),  
810 1177-1196.
- 811 Bensen, G. D., M. H. Ritzwoller, M. P. Barmin, A. L. Levshin, F. Lin, M. P. Moschetti, N. M. Shapiro,  
812 and Y. Yang (2007), Processing seismic ambient noise data to obtain reliable broad-band surface  
813 wave dispersion measurements, *Geophys. J. Int.*, *169*, 1239-1260, doi: 1210.1111/j.1365-  
814 1246X.2007.03374.x.

- 815 Brown, D., S. Llana-Funez, R. Carbonell, J. Alvarez-Marron, D. Marti, and M. Salisbury (2009),  
816 Laboratory measurements of P-wave and S-wave velocities across a surface analog of the  
817 continental crust–mantle boundary: Cabo Ortegal, Spain, *Earth Planet. Sci. Lett.*, 285(1–2), 27-38.
- 818 Burov, E., C. Jaupart, and J. C. Mareschal (1998), Large-scale crustal heterogeneities and lithospheric  
819 strength in cratons, *Earth Planet. Sci. Lett.*, 164(1-2), 205-219.
- 820 Cannon, W. F., et al. (1989), The North American Midcontinent Rift beneath Lake Superior from  
821 GLIMPCE seismic reflection profiling, *Tectonics*, 8(2), 305-332.
- 822 Cassidy, J. F. (1995), Review: Receiver function studies in the southern Canadian Cordillera, *Can. J.*  
823 *Earth Sci.*, 32, 1514-1519.
- 824 Catchings, R. D., and W. D. Mooney (1991), Basin and Range crustal and upper mantle structure,  
825 northwest to central Nevada, *J. Geophys. Res.*, 96(B4), 6247-6267.
- 826 Cheng, L. Z., J. C. Mareschal, C. Jaupart, F. Rolandone, C. Gariépya, and M. Radigon (2002),  
827 Simultaneous inversion of gravity and heat flow data: constraints on thermal regime, rheology and  
828 evolution of the Canadian Shield crust, *J. Geodyn.*, 34, 11-30, doi:10.1016/S0264-  
829 3707(1001)00082-00085.
- 830 Christensen, N. I. (1996), Poisson's ratio and crustal seismology, *J. Geophys. Res.*, 101, 3139-3156.
- 831 Christensen, N. I., and W. D. Mooney (1995), Seismic velocity structure and composition of the  
832 continental crust: A global view, *J. Geophys. Res.*, 100, 9761-9788.
- 833 Clowes, R. M., P. T. C. Hammer, G. Fernandez-Viejo, and J. K. Welford (2005), Lithospheric structure  
834 in northwestern Canada from Lithoprobe seismic refraction and related studies; a synthesis, *Can. J.*  
835 *Earth Sci.*, 42(6), 1277-1293.
- 836 Clowes, R. M., A. G. Green, C. J. Yorath, E. R. Kanasewich, G. F. West, and G. D. Garland (1984),  
837 LITHOPROBE - a national program for studying the third dimension of geology, *J. Can. Soc. Exp.*  
838 *Geophys.*, 20, 23-39.

- 839 Cook, F. (2002), Fine structure of the continental reflection Moho, *Geol. Soc. Am. Bull.*, *114*(1), 64-79.
- 840 Cook, F. A., D. J. White, A. G. Jones, D. W. S. Eaton, J. Hall, and R. M. Clowes (2010), How the crust  
841 meets the mantle; Lithoprobe perspectives on the Mohorovicic discontinuity and crust-mantle  
842 transition, *Can. J. Earth Sci.*, *47*(4), 315-351, doi:310.1139/E1109-1076.
- 843 Currie, C. A., and R. D. Hyndman (2006), The thermal structure of subduction zone back arcs, *J.*  
844 *Geophys. Res.*, *111*, B08404, doi:08410.01029/02005JB004024.
- 845 Currie, C. A., J. F. Cassidy, R. D. Hyndman, and M. G. Bostock (2004), Shear wave anisotropy beneath  
846 the Cascadia subduction zone and western North American craton, *Geophys. J. Int.*, *157*, 341-353,  
847 doi: 310.1111/j.1365-1246X.2004.02175.x.
- 848 Dalton, C. A., G. Ekström, and A. M. Dziewonski (2009), Global seismological shear velocity and  
849 attenuation: A comparison with experimental observations, *Earth Planet. Sci. Lett.*, *284*, 65-75,  
850 doi:10.1016/j.epsl.2009.1004.1009.
- 851 Darbyshire, F. A. (2005), Upper mantle structure of Arctic Canada from Rayleigh wave dispersion,  
852 *Tectonophysics*, *405*, 1-23.
- 853 Darbyshire, F. A., D. W. Eaton, A. W. Frederiksen, and L. Ertolahti (2007), New insights into the  
854 lithosphere beneath the Superior Province from Rayleigh wave dispersion and receiver function  
855 analysis, *Geophys. J. Int.*, *169*, 1043-1068, doi: 1010.1111/j.1365-1246X.2006.03259.x.
- 856 Dunkin, J. W. (1965), Computation of modal solutions in layered, elastic media at high frequencies,  
857 *Bull. Seismol. Soc. Am.*, *55*, 335-358.
- 858 Dziewonski, A. M., and D. L. Anderson (1981), Preliminary reference Earth model, *Phys. Earth*  
859 *Planet. Inter.*, *25*, 297-356.
- 860 Eakin, C. M., M. Obrebski, R. M. Allen, D. C. Boyarko, M. R. Brudzinski, and R. Porritt (2010),  
861 Seismic anisotropy beneath Cascadia and the Mendocino triple junction; interaction of the  
862 subducting slab with mantle flow, *Earth Planet. Sci. Lett.*, *297*(3-4), 627-632.

- 863 Flück, P., R. D. Hyndman, and C. Lowe (2003), Effective elastic thickness  $T_e$  of the lithosphere in  
864 western Canada, *J. Geophys. Res.*, *108*(B9), 2430, doi:2410.1029/2002JB002201.
- 865 Fountain, D. M., and N. Christensen (Eds.) (1989), *Composition of the continental crust and upper*  
866 *mantle: a review*, 711-742 pp., GSA Mem.
- 867 Frederiksen, A. W., M. G. Bostock, J. C. VanDecar, and J. F. Cassidy (1998), Seismic structure of the  
868 upper mantle beneath the northern Canadian Cordillera from teleseismic travel-time inversion,  
869 *Tectonophysics*, *294*, 43-55.
- 870 Frederiksen, A. W., S.-K. Miong, F. A. Darbyshire, D. W. Eaton, S. Rondenay, and S. Sol (2007),  
871 Lithospheric variations across the Superior Province, Ontario, Canada: Evidence from tomography  
872 and shear wave splitting, *J. Geophys. Res.*, *112*, B07318, doi:07310.01029/02006JB004861.
- 873 Fulton, R. J. (1989), *Quaternary Geology of Canada and Greenland: Maps*, International Specialized  
874 Book Service Incorporated.
- 875 Green, D. H., and A. E. Ringwood (1972), A comparison of recent experimental data on the gabbro-  
876 garnet granulite-eclogite phase transition, *J. Geology*, *80*(3), 277-288. doi:210.1086/627731.
- 877 Guillou-Frottier, L., C. Jaupart, J. C. Mareschal, C. Gariépy, G. Bienfait, L. Z. Cheng, and R. Lapointe  
878 (1996), High heat flow in the trans-Hudson Orogen, Central Canadian Shield, *Geophys. Res. Lett.*,  
879 *23*(21), 3027-3030, doi:3010.1029/3096GL02895.
- 880 Hyndman, R. D., and T. S. Lewis (1999), Geophysical consequences of the Cordillera-Craton thermal  
881 transition in southwestern Canada, *Tectonophysics*, *306*, 397-422, doi:310.1016/S0040-  
882 1951(1099)00068-00062.
- 883 Hyndman, R. D., and C. A. Currie (2011), Why is the North America Cordillera high? Hot backarcs,  
884 thermal isostasy, and mountain belts, *Geology*, *39*(8), 783-786, doi:710.1130/G31998.31991.
- 885 Hyndman, R. D., C. A. Currie, S. Mazzotti, and A. Frederiksen (2009), Temperature control of  
886 continental lithosphere elastic thickness,  $T_e$  vs  $V_s$ , *Earth Planet. Sci. Lett.*, *277*, 539-548.

- 887 Hyndman, R. D., P. Flück, S. Mazzotti, T. J. Lewis, J. Ristau, and L. Leonard (2005), Current tectonics  
888 of the northern Canadian Cordillera, *Can. J. Earth Sci.*, *42*, 1117-1136, doi:1110.1139/E1105-1023.
- 889 Ito, K., and G. C. Kennedy (1971), An experimental study of the basalt–garnet granulite–eclogite  
890 transition, in *The Earth beneath the continents*, edited by J. G. Heacock, pp. 303-314, AGU  
891 Geophysical Monograph 14, Washington, D. C.
- 892 Jones, A. G., and I. J. Ferguson (2001), The electric Moho, *Nature*, *409*(6818), 331-333.
- 893 Klemperer, S. L., T. A. Hauge, E. C. Hauser, J. E. Oliver, and C. J. Potter (1986), The Moho in the  
894 northern Basin and Range province, Nevada, along the COCORP 400N seismic reflection transect,  
895 *Geol. Soc. Am. Bull.*, *97*(5), 603-618.
- 896 Lebedev, S., and R. D. van der Hilst (2008), Global upper-mantle tomography with the automated  
897 multimode inversion of surface and S-wave forms, *Geophys. J. Int.*, *173*, 505-518, doi:  
898 10.1111/j.1365-1246X.2008.03721.x.
- 899 Lebedev, S., J. M. C. Adam, and T. Meier (2013), Mapping the Moho with seismic surface waves: A  
900 review, resolution analysis, and recommended inversion strategies, *Tectonophysics*, *in press*.
- 901 Lekic, V., and B. Romanowicz (2011), Tectonic regionalization without a priori information; a cluster  
902 analysis of upper mantle tomography, *Earth Planet. Sci. Lett.*, *308*(1-2), 151-160.
- 903 Leveque, J.-J., L. Rivera, and G. Wittlinger (1993), On the use of the checker-board test to assess the  
904 resolution of tomographic inversion, *Geophys. J. Int.*, *115*, 313-318.
- 905 Levin, V., W. Menke, and J. Park (1999), Shear wave splitting in the Appalachians and the Urals: A  
906 case for multilayered anisotropy, *J. Geophys. Res.*, *104*, 17,975-917,993.
- 907 Levshin, A. L., and M. H. Ritzwoller (2001), Automated detection, extraction, and measurement of  
908 regional surface waves, *Pure Appl. Geophys.*, *158*(8), 1531-1545.
- 909 Lin, F.-C., M. P. Moschetti, and M. H. Ritzwoller (2008), Surface wave tomography of the Western  
910 United States from ambient seismic noise; Rayleigh and Love wave phase velocity maps, *Geophys.*

- 911 *J. Int.*, 173(1), 281-298, doi:210.1111/j.1365-1246X.2008.03720.x.
- 912 Lin, F.-C., M. H. Ritzwoller, J. Townend, S. Bannister, and M. Savage (2007), Ambient noise Rayleigh  
913 wave tomography of New Zealand, *Geophys. J. Int.*, doi:10.1111/j.1365-1246X.2007.03414x.
- 914 Ma, K.-F., Y.-Y. Lin, S.-J. Lee, J. Mori, and E. E. Brodsky (2012), Isotropic events observed with a  
915 borehole array in the Chelungpu fault zone, Taiwan, *Science*, 337(459), 459-463,  
916 doi:410.1126/science.1222119.
- 917 Mareschal, J. C., C. Jaupart, F. Rolandone, C. Gariépy, C. M. R. Fowler, G. Bienfait, C. Carbonne, and  
918 R. Lapointe (2005), Heat flow, thermal regime, and elastic thickness of the lithosphere in the Trans-  
919 Hudson Orogen, *Can. J. Earth Sci.*, 42(4), 517-532, doi:510.1139/e1104-1088.
- 920 Mazzotti, S., and R. D. Hyndman (2002), Yakutat collision and strain transfer across the northern  
921 Canadian Cordillera, *Geology*, 30, 495-498.
- 922 Mercier, J.-P., M. G. Bostock, J. F. Cassidy, K. Dueker, J. B. Gaherty, E. J. Garnero, J. Revenaugh, and  
923 G. Zandt (2009), Body-wave tomography of western Canada, *Tectonophysics*, 475, 480-492,  
924 doi:410.1016/j.tecto.2009.1005.1030.
- 925 Mohorovicic, A. (1910), Das Beben Vom 8. x. 1909, *Jahrbuch Meteorologie Observatorie Zagrab*, Vol.  
926 9, 1-63.
- 927 Mooney, W. D. (1987), Seismology of the continental crust and upper mantle, *Rev. Geophys.*, 25, 1168-  
928 1176.
- 929 Mooney, W. D., and T. M. Brocher (1987), Coincident seismic reflection/refraction studies of the  
930 continental lithosphere: a global review, *Rev. Geophys.*, 25, 723-742.
- 931 Mooney, W. D., G. Laske, and T. G. Masters (1998), CRUST 5.1: A global crustal model at 5° x 5°, *J.*  
932 *Geophys. Res.*, 103, 727-747.
- 933 Moores, E. M. (1982), Origin and emplacement of ophiolites, *Rev. Geophys. Space Phys.*, 20(4), 735-  
934 760.

- 935 Moschetti, M. P., M. H. Ritzwoller, F. C. Lin, and Y. Yang (2010a), Crustal shear wave velocity  
936 structure of the Western United States inferred from ambient seismic noise and earthquake data, *J.*  
937 *Geophys. Res.*, *115*(B10), B10306, doi:10.1029/2010JB007448.
- 938 Moschetti, M. P., M. H. Ritzwoller, F. Lin, and Y. Yang (2010b), Seismic evidence for widespread  
939 Western-US deep-crustal deformation caused by extension, *Nature*, *464*(7290), 885-889.
- 940 Nettles, M., and A. M. Dziewonski (2008), Radially anisotropic shear velocity structure of the upper  
941 mantle globally and beneath North America, *J. Geophys. Res.*, *113*, B02303,  
942 doi:02310.01029/02006JB004819.
- 943 Okulitch, A. V., and H. Trettin (1991), Late Cretaceous to Early Tertiary deformation, Arctic Islands, in  
944 *Geology of the Innuitian Orogen and Arctic Platform of Canada and Greenland*, edited by H. P.  
945 Trettin, pp. 469-489, Geol. Surv. Canada, Ottawa.
- 946 Pawlak, A., D. W. Eaton, I. D. Bastow, J.-M. Kendall, G. Helffrich, J. Wookey, and D. Snyder (2010),  
947 Crustal structure beneath Hudson Bay from ambient-noise tomography: implications for basin  
948 formation, *Geophys. J. Int.*, *181*, 65-82, doi: 10.1111/j.1365-1246X.2010.04828.x.
- 949 Perry, H. K. C., D. W. S. Eaton, and A. M. Forte (2002), LITH5.0: a revised crustal model for Canada  
950 based on Lithoprobe results, *Geophys. J. Int.*, *150*, 285-294.
- 951 Perry, H. K. C., C. Jaupart, J.-C. Mareschal, and G. Bienfait (2006), Crustal heat production in the  
952 Superior Province, Canadian Shield, and in North America inferred from heat flow data, *J.*  
953 *Geophys. Res.*, *111*, B04401, doi:04410.01029/02005JB003893.
- 954 Richter, C. F. (1958), *Elementary Seismology*, 712 pp., Freeman, San Francisco, Calif.
- 955 Rieger, D. M., and J. Park (2010), USArray observations of quasi-Love surface wave scattering;  
956 orienting anisotropy in the Cascadia plate boundary, *J. Geophys. Res.*, *115*(B5), B05306,  
957 doi:05310.01029/02009jb006754.
- 958 Ritzwoller, M. H., F.-C. Lin, and W. Shen (2011), Ambient noise tomography with a large seismic



- 959 array, *Comptes Rendus Geoscience*, 343, 558-570, doi:510.1016/j.crte.2011.1003.1007.
- 960 Sabra, K. G., P. Gerstoft, P. Roux, W. A. Kuperman, and M. C. Fehler (2005), Surface wave  
961 tomography from microseisms in Southern California, *Geophys. Res. Lett.*, 32(14), L14311,  
962 doi:14310.11029/12005GL023155.
- 963 Sambridge, M. (1999a), Geophysical Inversion with a Neighbourhood Algorithm -II. Appraising the  
964 ensemble, *Geophys. J. Int.*, 138, 727-746.
- 965 Sambridge, M. (1999b), Geophysical inversion with a neighbourhood algorithm - I. Searching a  
966 parameter space, *Geophys. J. Int.*, 138, 479-494.
- 967 Shapiro, N. M., M. H. Ritzwoller, P. Molnar, and V. Levin (2004a), Thinning and flow of Tibetan crust  
968 constrained by seismic anisotropy, *Science*, 305, 233-236. doi:210.1126/science.1098276.
- 969 Shapiro, N. M., M. H. Ritzwoller, J. C. Mareschal, and C. Jaupart (2004b), Lithospheric structure of the  
970 Canadian Shield inferred from inversion of surface-wave dispersion with thermodynamic a priori  
971 constraints, *Geol. Soc. London Special Pub.*, 239, 175-194,  
972 doi:110.1144/GSL.SP.2004.1239.1101.1112.
- 973 Shapiro, N. M., M. Campillo, L. Stehly, and M. H. Ritzwoller (2005), High-resolution surface-wave  
974 tomography from ambient seismic noise, *Science*, 307(5715), 1615-1618.
- 975 Shen, W., M. H. Ritzwoller, and V. Schulte-Pelkum (2013), A 3-D model of the crust and uppermost  
976 mantle beneath the Central and Western US by joint inversion of receiver functions and surface  
977 wave dispersion, *J. Geophys. Res. Solid Earth*, 118, 1-15, doi:10.1029/2012JB009602.
- 978 Simmons, N. A., A. M. Forte, L. Boschi, and S. P. Grand (2010), GyPSuM; a joint tomographic model  
979 of mantle density and seismic wave speeds, *J. Geophys. Res.*, 115(B12), B12310,  
980 doi:12310.11029/12010JB007631.
- 981 Simons, F., R. D. van der Hilst, J.-P. Montagner, and A. Zielhuis (2002), Multimode Rayleigh wave  
982 inversion for heterogeneity and azimuthal anisotropy of the Australian upper mantle, *Geophys. J.*

- 983        *Int.*, 151, 738-754.
- 984    Stehly, L., M. Campillo, and N. M. Shapiro (2006), A study of the seismic noise from its long-range  
985        correlation properties, *J. Geophys. Res.*, 111(B10), B10306, doi:10.1029/2005JB004237.
- 986    Steinhart, J. S. (1967), Mohorovicic discontinuity, in *International dictionary of geophysics*, edited by  
987        S. K. Runcorn, pp. 991–994, Pergamon Press, Oxford, UK.
- 988    Tibuleac, I. M., D. H. von Seggern, J. G. Anderson, and J. N. Louie (2011), Computing Green's  
989        functions from ambient noise recorded by accelerometers and analog, broadband, and narrow-band  
990        seismometers, *Seismol. Res. Lett.*, 82(5), 661-675, doi:10.1785/gssrl.1782.1785.1661.
- 991    van der Lee, S., and A. Frederiksen (2005), Surface wave tomography applied to the North American  
992        upper mantle, in *Seismic Earth: Array Analysis of Broadband Seismograms*, edited by G. Nolet, pp.  
993        67-80, AGU Geophysical Monograph 157, Washington, DC.
- 994    Vincent, J. (1989), Quaternary geology of the southeastern Canadian Shield, *Quaternary geology of*  
995        *Canada and Greenland*, 1, 249-275.
- 996    Wang, Y., and J. Mareschal (1999), Elastic thickness of the lithosphere in the Central Canadian Shield,  
997        *Geophys. Res. Lett.*, 26(19), 3033-3036, doi:10.1029/1999GL010806.
- 998    Wapenaar, K., D. Draganov, and J. O. A. Robertsson (2008), *Seismic Interferometry: History and*  
999        *Present Status*, 628 pp., Soc. of Explor. Geophys., Tulsa, OK.
- 1000    Wathelet, M. (2005), Array recordings of ambient vibrations: surface wave inversion, Ph.D. thesis,  
1001        Faculté des Sciences Appliquées.
- 1002    Wathelet, M. (2008), An improved neighborhood algorithm: Parameter conditions and dynamic scaling,  
1003        *Geophys. Res. Lett.*, 35, doi:10.1029/2008GL033256.
- 1004    Wheeler, J. O., P. F. Hoffman, K. D. Card, A. Davidson, B. V. Sanford, A. V. Okulitch, and W. R. Roest  
1005        (1997), Geological Map of Canada, *Map D1860A*.
- 1006    Williams, H. (1979), Appalachian Orogen in Canada, *Can. J. Earth Sci.*, 16(3), 792-807.

1007 Wu, P. (1991), Flexure of lithosphere beneath the Alberta foreland basin: evidence of an eastward  
1008 stiffening continental lithosphere, *Geophys. Res. Lett.*, 18(3), 451-454.

1009 Yuan, H., and B. Romanowicz (2010), Lithospheric layering in the North American Craton, *Nature*,  
1010 466(7310), 1063-1068, doi:10.1038/nature09332.

1011 Zhou, L., J. Xie, W. Shen, Y. Zheng, Y. Yang, H. Shi, and M. H. Ritzwoller (2012), The structure of the  
1012 crust and uppermost mantle beneath south China from ambient noise and earthquake tomography,  
1013 *Geophys. J. Int.*, 189(3), 1565-1583, doi: 1510.1111/j.1365-1246X.2012.05423.x.

1014  
1015 **Figure Caption**

1016 **Figure 1.** Topography map of Canada showing major geological and tectonic settings. Thick purple  
1017 lines mark the boundaries between the Canadian Shield, where the Archean craton is exposed, and  
1018 stable platforms, where sedimentary rocks are underlain by the craton. Thick red lines mark the  
1019 boundaries between stable platforms and orogenic belts. Jdf: Juan de Fuca plate; ExP: Explorer plate;  
1020 QCF: Queen Charlotte fault.

1021 **Figure 2.** Station distribution and ray path coverage of our dataset. The color of the ray path varies  
1022 with the inter-station distance (black indicates the longest paths, white the shortest) to better depict the  
1023 path density of different regions. Red triangles mark the location of stations discussed in the text and  
1024 subsequent figures.

1025 **Figure 3.** Representative examples of stacked cross-correlation functions from continuous ambient  
1026 seismic noise data. Locations of stations are shown in Figure 2.

1027 **Figure 4.** Representative examples of stacked cross-correlation functions using various amount of  
1028 ambient seismic noise (1 year: top trace; 3 years: middle trace; and 7 years: bottom trace). Notice that  
1029 the improvement in signal-to-noise ratio becomes marginal once the amount of data exceeds 3 years.  
1030 The result of frequency-time analysis (FTAN) is shown at the lower panel with the determined  
1031 dispersion curve shown in white.

1032 **Figure 5.** A comparison of the stacked cross-correlation functions (top trace), the symmetric  
1033 component of the cross-correlation function (middle trace), and the dispersion measurement (bottom  
1034 panel) for the station pair RLMT and NLWA. Our results (a) and those obtained from the IRIS Data  
1035 Management Center (b) are nearly identical.

1036 **Figure 6.** Surface wave tomography inversion results using ambient seismic noise data for the periods  
1037 of 10 s (a), 35 s (b), and 50 s (c). For each period, the phase and group velocity distribution are shown  
1038 at the top panels. The bottom panel shows the corresponding resolution length as determined from the  
1039 spike-perturbation test (left) and the depth sensitivity kernel (calculated at the location of 55°N,  
1040 110°W).

1041 **Figure 7.** Examples of 1D shear-velocity inversion for 4 representative grid points. The phase and  
1042 group velocity dispersion curves are shown at the top and middle panels, respectively. The observed  
1043 measurements are marked by black plus symbols, whereas the synthetics corresponding to the best-  
1044 fitting model is shown in pink. The Neighbourhood Algorithm inversion results are shown at the  
1045 bottom panel. The color of the model space represents the density distribution of samples. The solid  
1046 and dashed black lines in the middle correspond to the weighted average and the best-fitting models,  
1047 respectively. Red dashed lines mark the sampled model space.

1048 **Figure 8.** Distribution of the root-mean-square (RMS) misfit of our Neighbourhood Algorithm  
1049 inversion for the shear-velocity structure of Canada and adjacent regions.

1050 **Figure 9.** Pseudo-3D tomography of Canada and its adjacent regions. The distribution of shear velocity  
1051 at the depths of 5 km (a), 25 km (b), and 50 km (c) is displayed in color with red and blue  
1052 corresponding to low and high values, respectively. White dashed lines on the 50-km image mark the  
1053 location of cross sections shown in Figure 10, whereas small red circles and crosses correspond to the  
1054 locations of velocity profiles shown in Figures 6 and 12, respectively.

1055 **Figure 10.** Three east–west (A–A', B–B', and C–C') and three north–south (1–1', 2–2', 3–3') cross

1056 sections showing pseudo-3D tomography of Canada. Color scale is the same as that in Figure 9.

1057 Vertical gradient of the  $V_s$  distribution is normalized and displayed as gray-scale shading overlaying the  
 1058 velocity images. The black and red lines correspond to the 50% and 85%  $V_s$  increase from crust to  
 1059 upper mantle, respectively, and effectively define the depth range of the crust–mantle transition.

1060 Geographic locations of the cross sections are marked in Figure 9c.

1061 **Figure 11.** A schematic illustration on how the crust–mantle transition is characterized in this study.

1062 The lower crust shear velocity and the uppermost mantle shear velocities define the 0% and 100% of  
 1063 the  $V_s$  increase across the transition. Locations where the  $V_s$  increase reaches 50% and 85% are marked  
 1064 by blue and black crosses, respectively. Depth and shear velocity at the blue cross is inferred to be  $Z_{50\%}$   
 1065 and  $V_{50\%}$ . Depth and shear velocity at the black cross is inferred to be  $Z_{85\%}$  and  $V_{85\%}$ .

1066 **Figure 12.** Cross sections showing the distribution of crust–mantle transition delineated from ambient  
 1067 noise tomography results (gray zone). Locations of the Moho discontinuity reported in the CRUST2.0  
 1068 and LITH5.0 models are plotted in dashed red and blue lines, respectively, for comparison.

1069 **Figure 13.** Physical properties of the crust–mantle transition beneath Canada and the adjacent regions.

1070 (a) Depth contours corresponding to 50% shear-velocity increase from crust to upper mantle. (b) Depth  
 1071 contours corresponding to 85% shear-velocity increase from crust to upper mantle. (c) Thickness of the  
 1072 crust–mantle transition, which is the depth difference between (a) and (b). (d) Shear velocity at which  
 1073 the amount of increase is 50% from crust to upper mantle. (e) Similar to (d) but the amount of increase  
 1074 is 85%. (f) Amount of shear-velocity contrast across the crust–mantle transition, defined as the  
 1075 difference between (d) and (e).

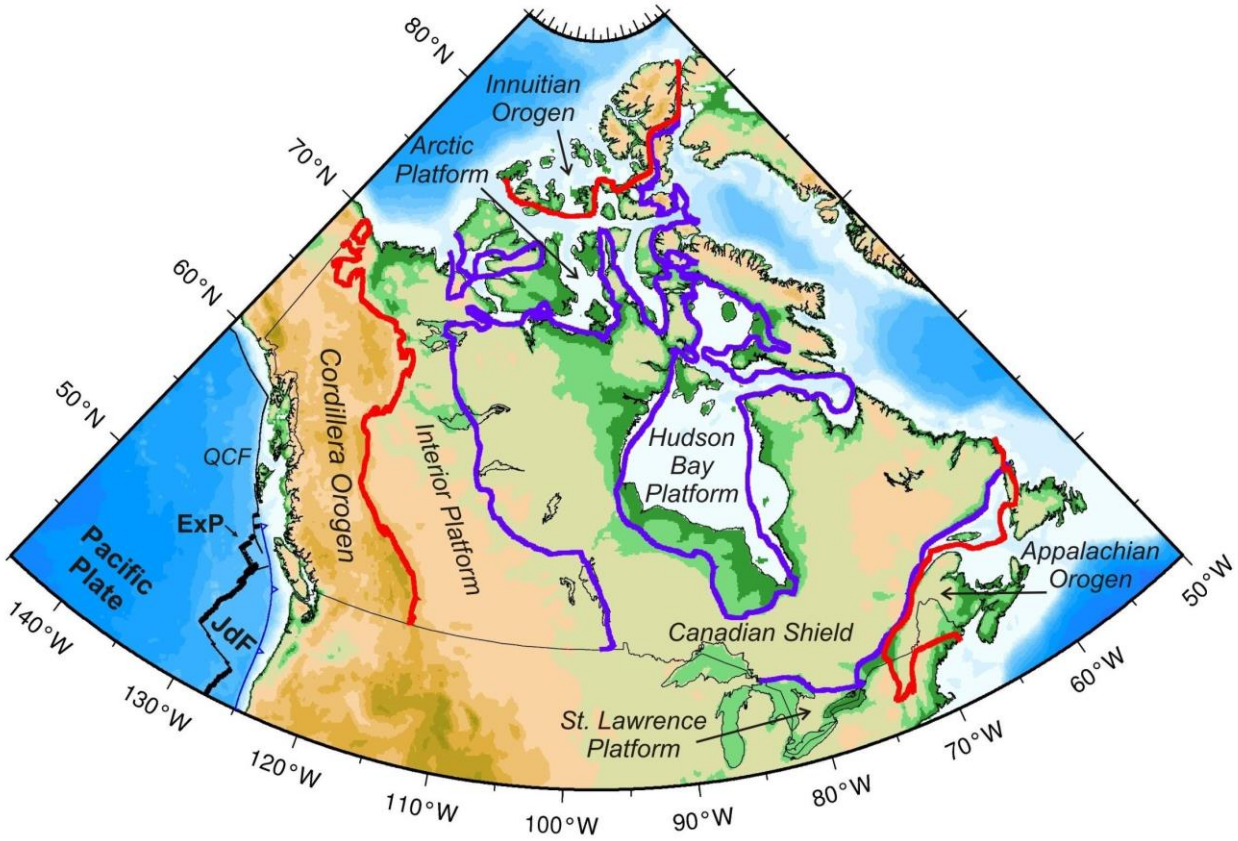
1076 **Figure 14.** Comparison of Lithoprobe seismic reflection profiles and the shear-velocity profiles of our  
 1077 tomography inversion at 10 selected grid nodes. The original Lithoprobe transect identifier is shown at  
 1078 the top of each reflection profile with the geographic coordinates of each grid node. The thick red and  
 1079 blue lines correspond to the weighted average and best-fitting models, respectively. Red circles mark

1080 the location of "ambient noise" Moho which is defined as the location where shear-velocity increases  
1081 by 85% from lower crust to upper mantle. Dashed orange lines mark the Moho depths in the LITH5.0  
1082 model that are primarily derived from Lithoprobe data. Thin blue lines mark the model uncertainty as  
1083 determined from forward modeling.

1084 **Figure 15.** Histograms showing the depth difference between the crustal model determined in this  
1085 study and two previous models, CRUST2.0 (left) and LITH5.0 (right).  $Z_{50\%}$ ,  $Z_{75\%}$ ,  $Z_{85\%}$ , and  $Z_{100\%}$   
1086 correspond to the depths where the increase of shear velocity is 50%, 75%, 85%, and 100% from the  
1087 lower crust to the uppermost mantle. The mean value (avg) of all samples is given near the top-right  
1088 corner of each plot. We use the  $Z_{85\%}$  as a proxy for the "ambient noise Moho" because it yields the least  
1089 overall difference with respect to both CRUST2.0 and LITH5.0 models.

1090 **Figure 16.** Histograms showing the velocity difference between the velocity model determined in this  
1091 study and two previous tomography models based on earthquake data, NA04 (left) and NA07 (right).  
1092 The top and bottom correspond to the depth of 70 and 90 km, respectively. Overall, our results are  
1093 slightly slower than those reported in previous models, as indicated by the mean value (avg) given near  
1094 the top-right corner of each plot. This systematic difference is likely due to the effect of radial  
1095 anisotropy in the upper mantle. See text for more details.

1096



1097

1098 Figure 1

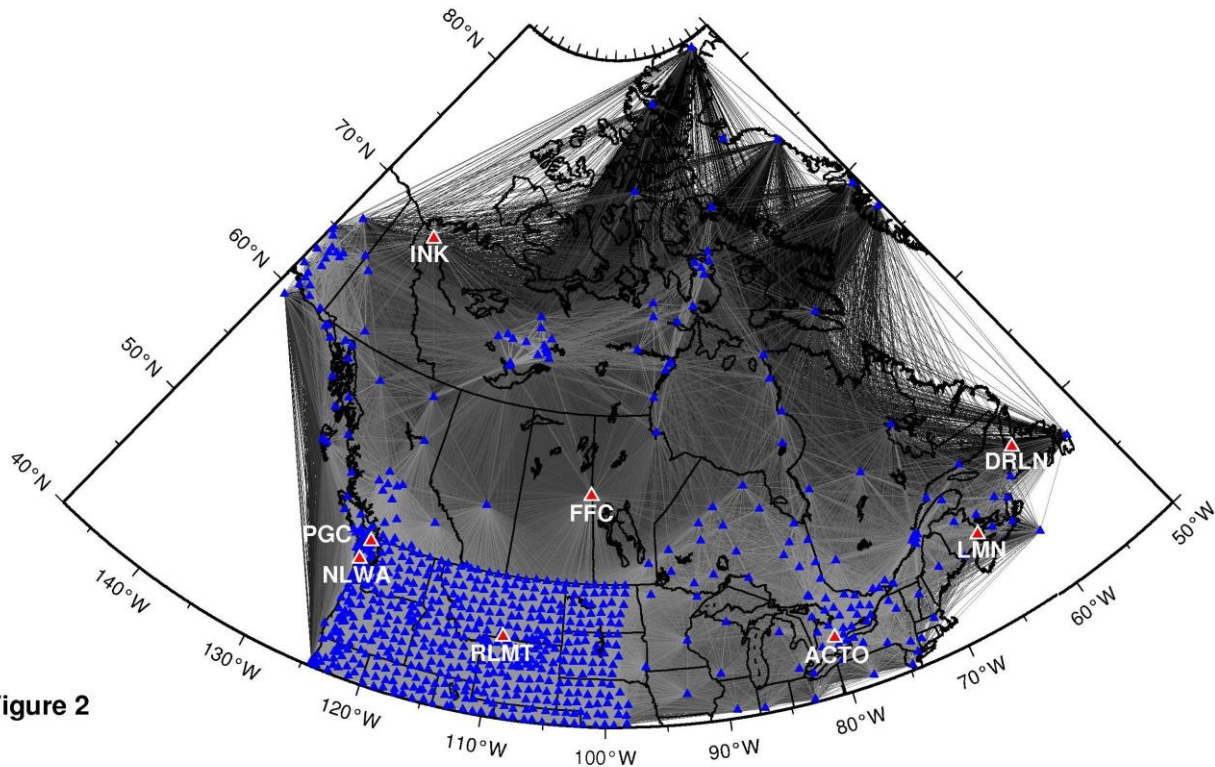
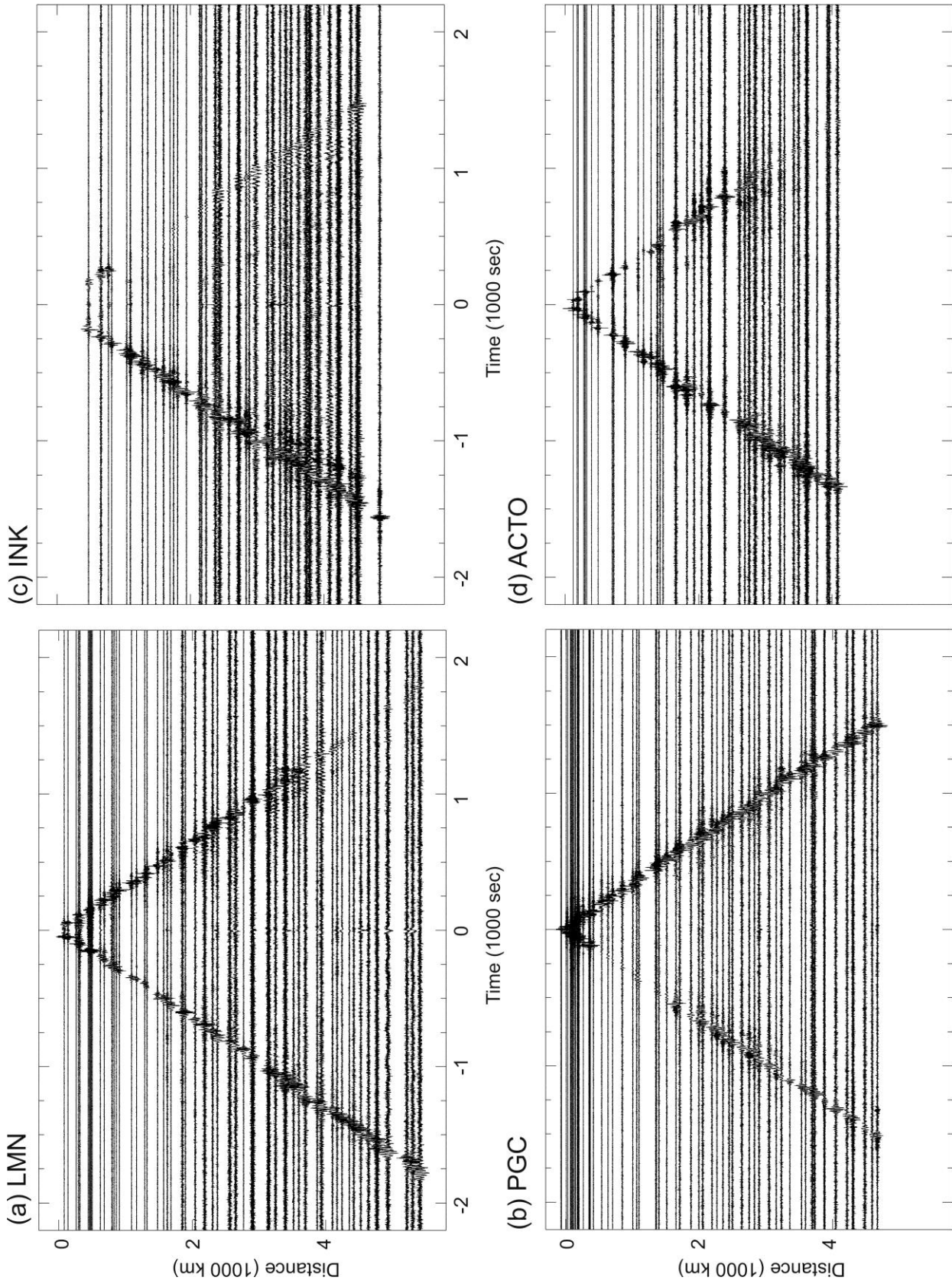


Figure 2

1099

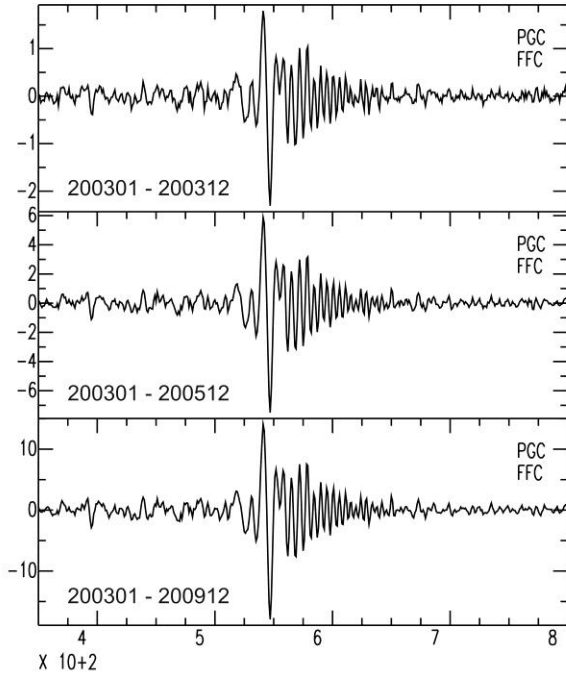


1100

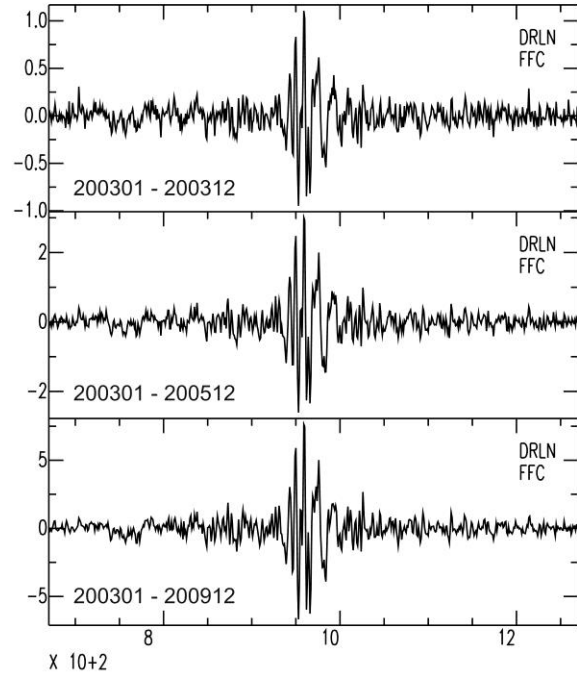
1101 Figure 3



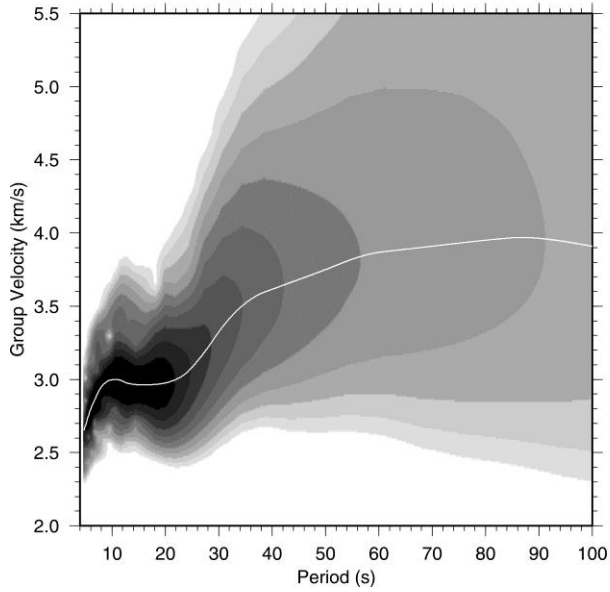
(a) Cross-Correlation Function



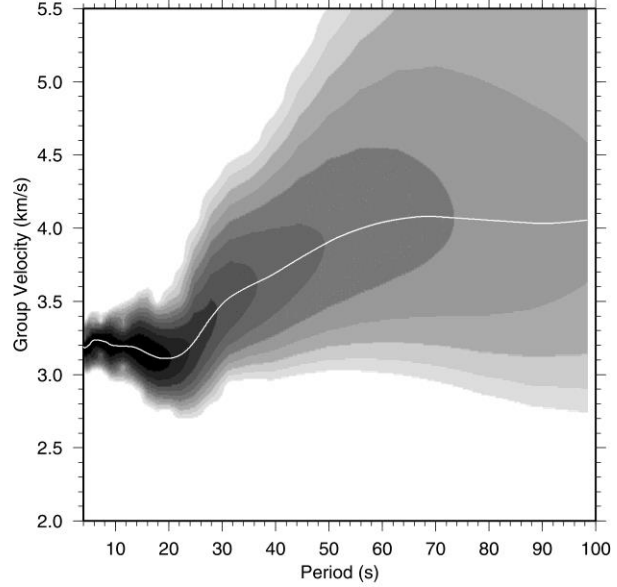
(b) Cross-Correlation Function



Dispersion Curve



Dispersion Curve

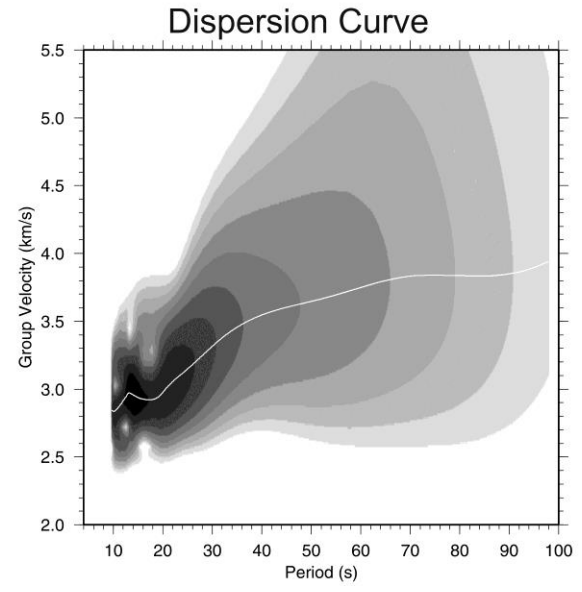
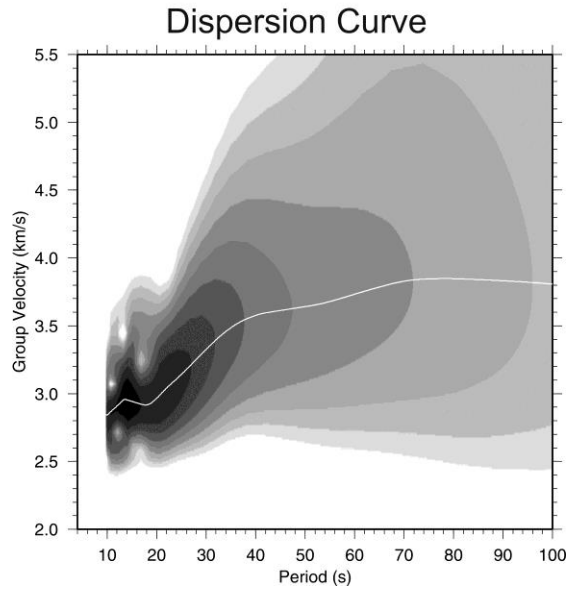
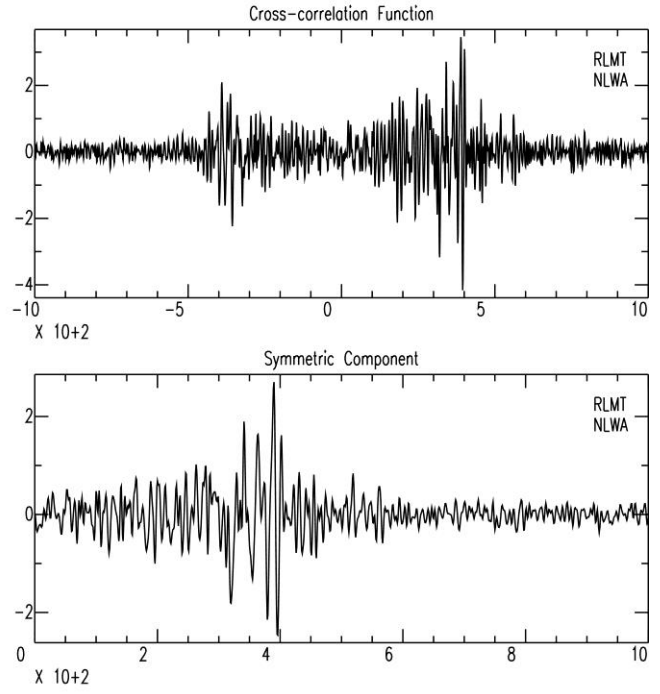
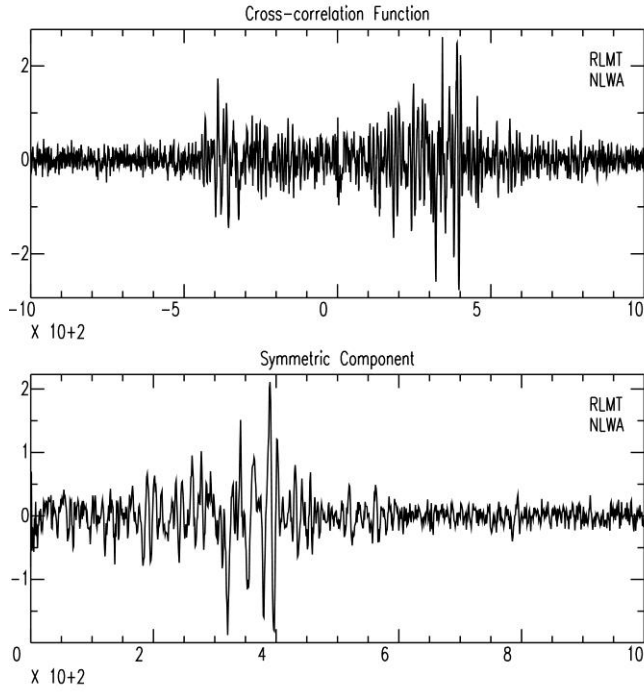


1102

1103 Figure 4

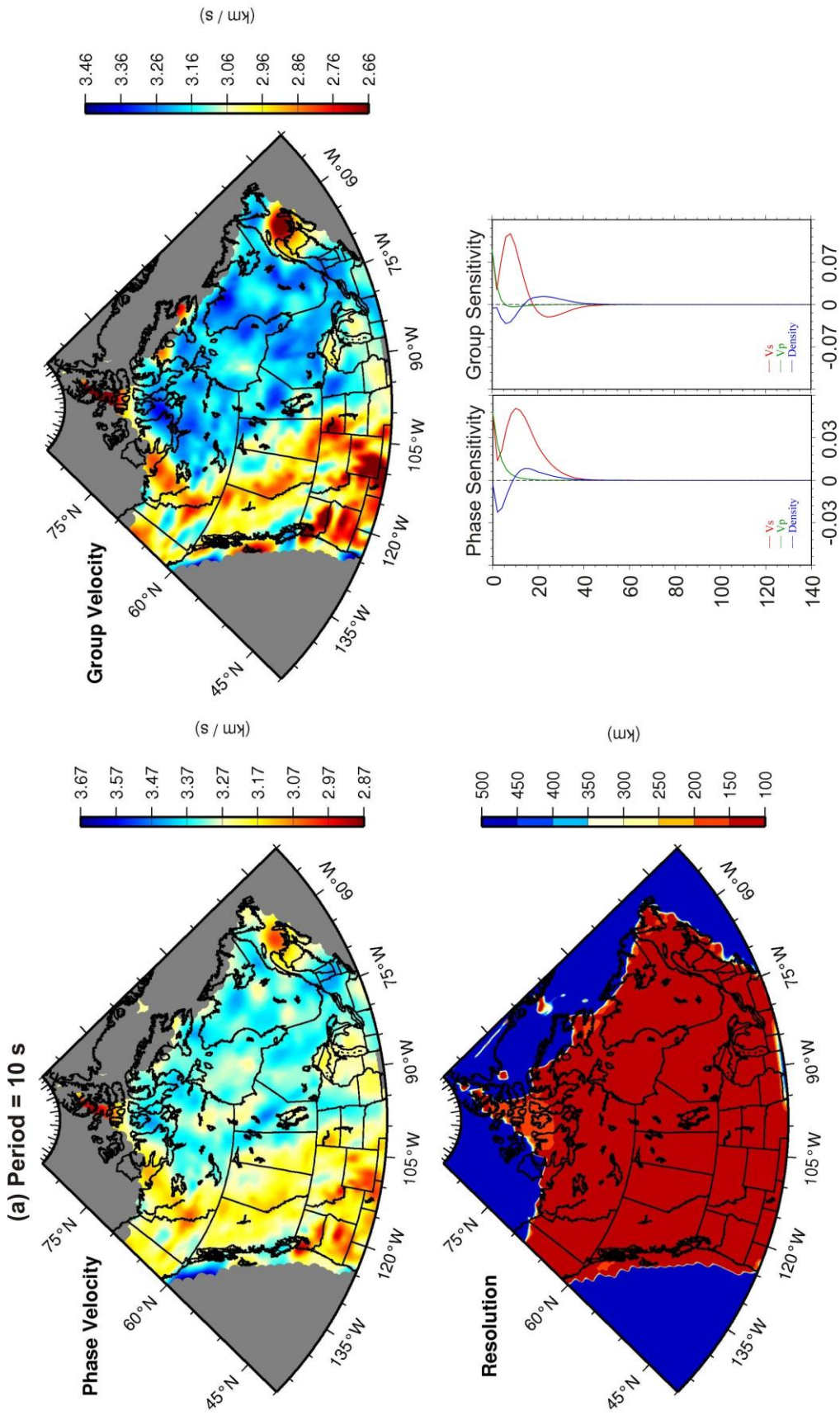
(a) This study (2003 - 2009)

(b) From IRIS DMC (2005 - 2010)



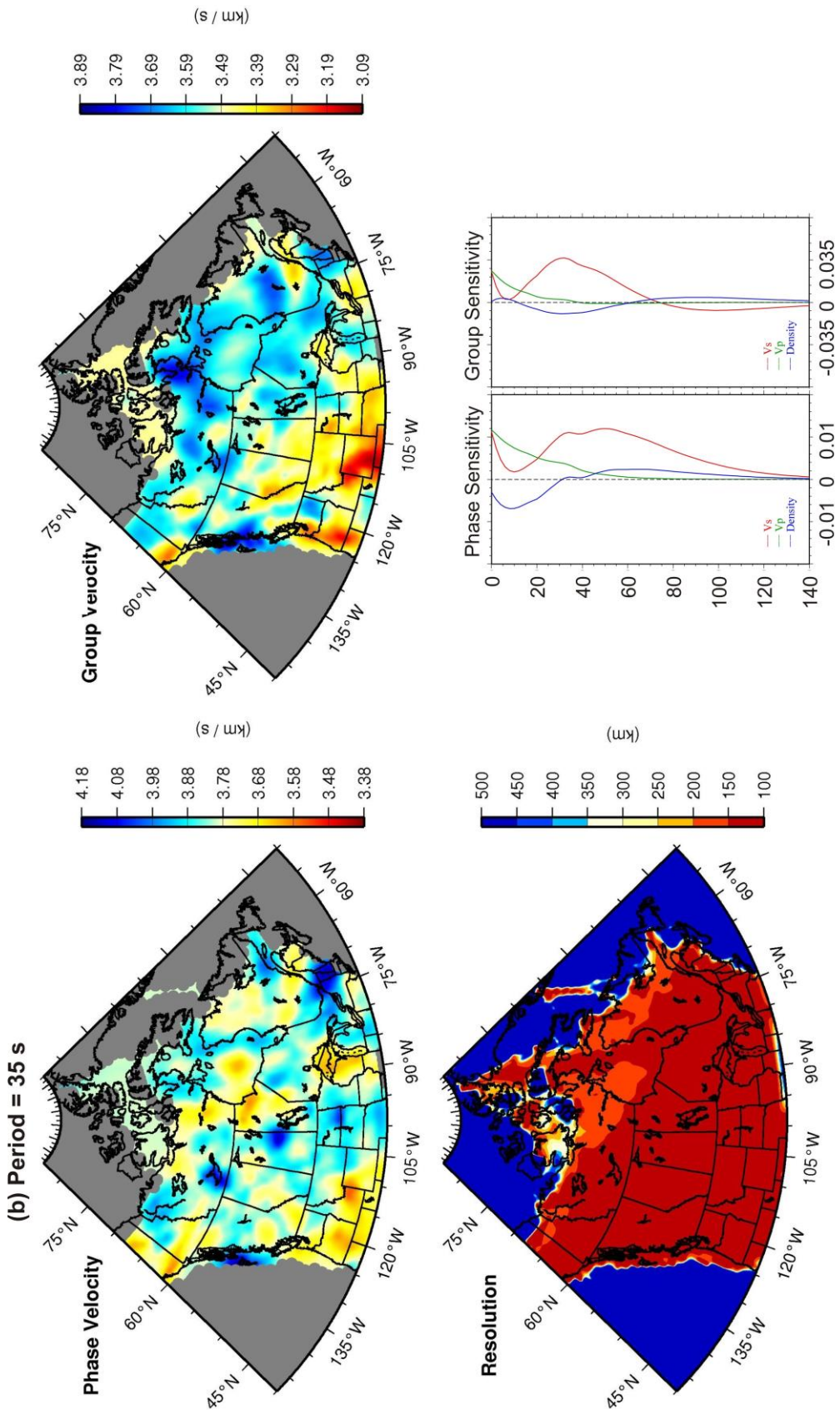
1104

1105 Figure 5



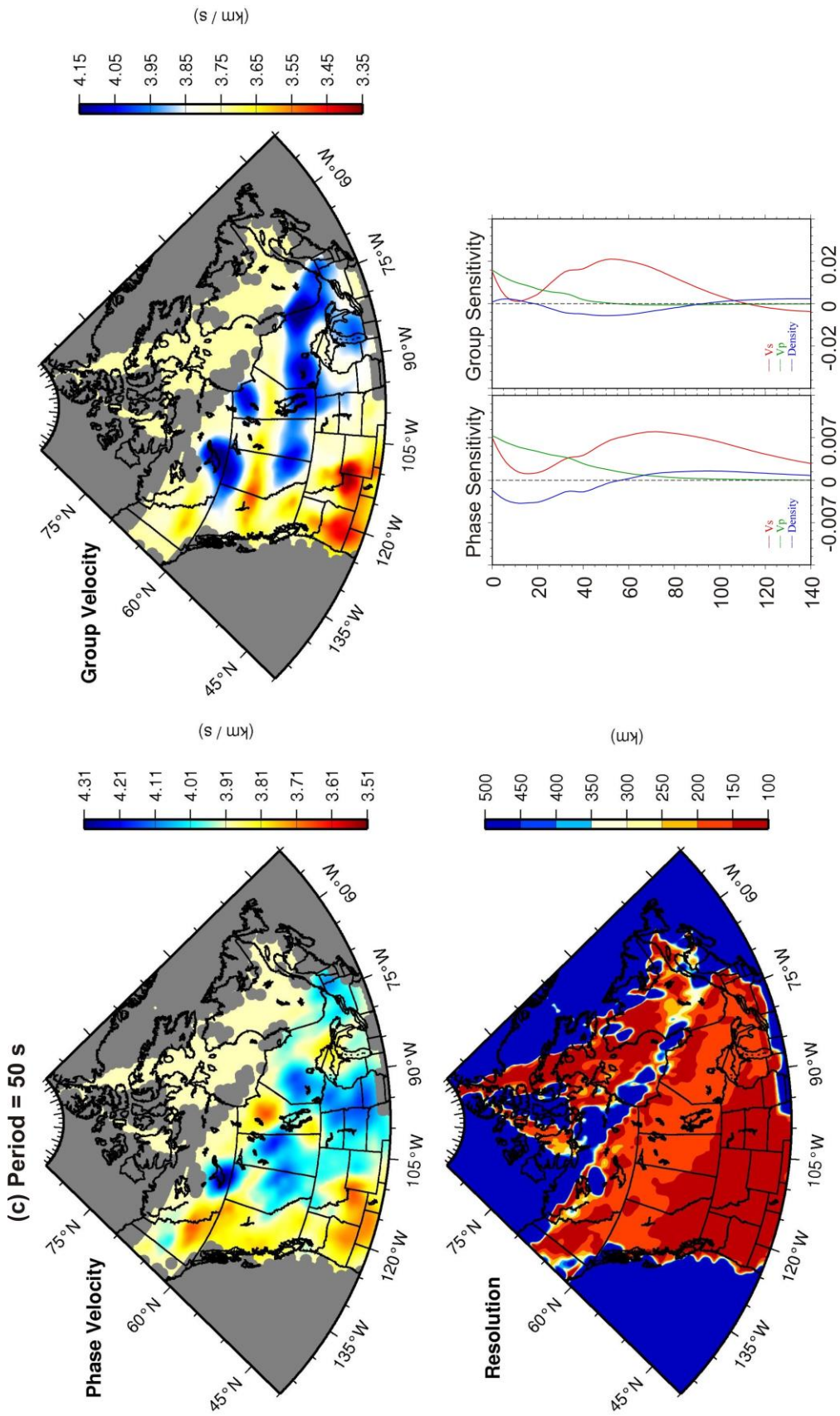
1106

1107 Figure 6a



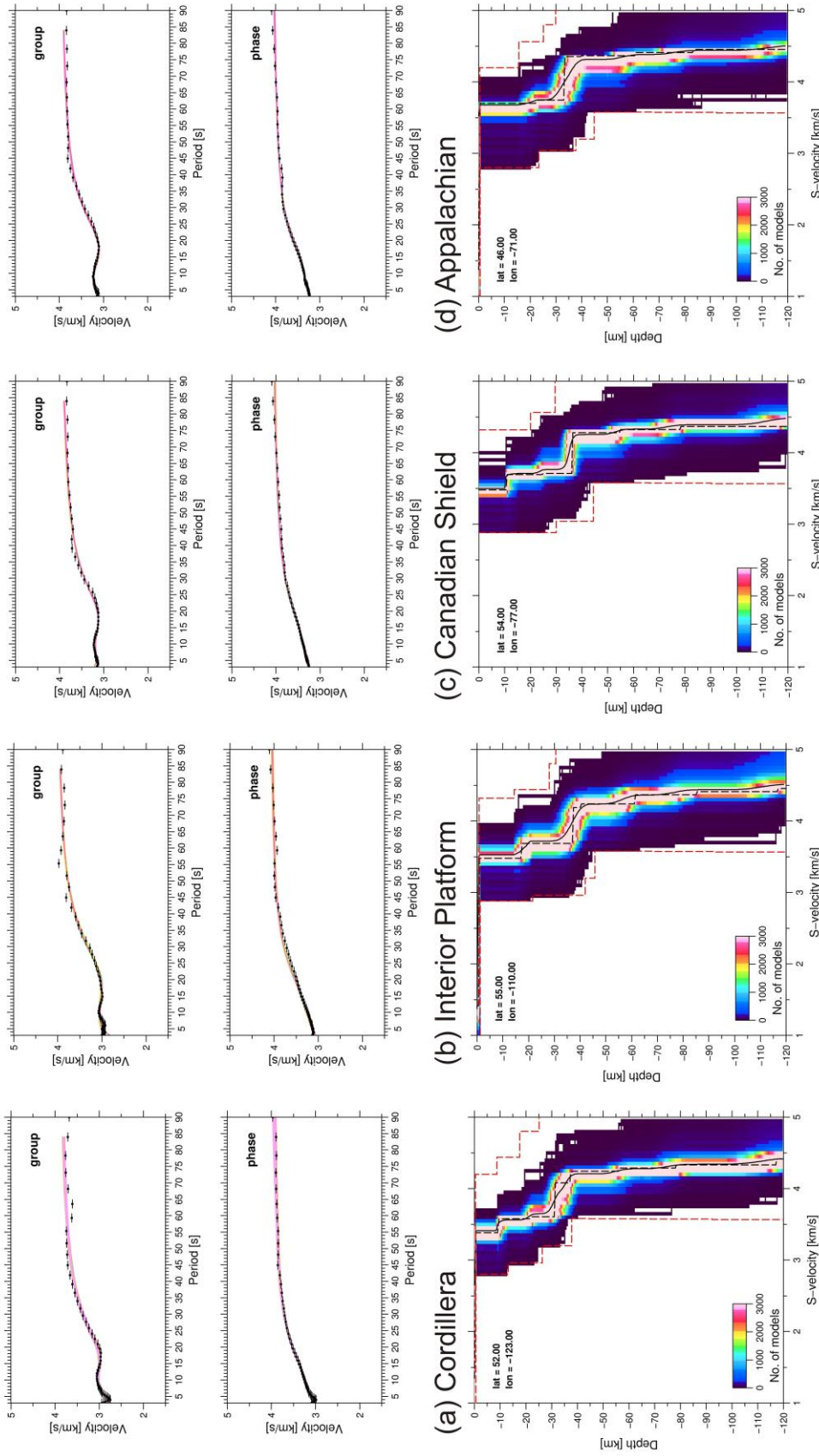
1108

1109 Figure 6b



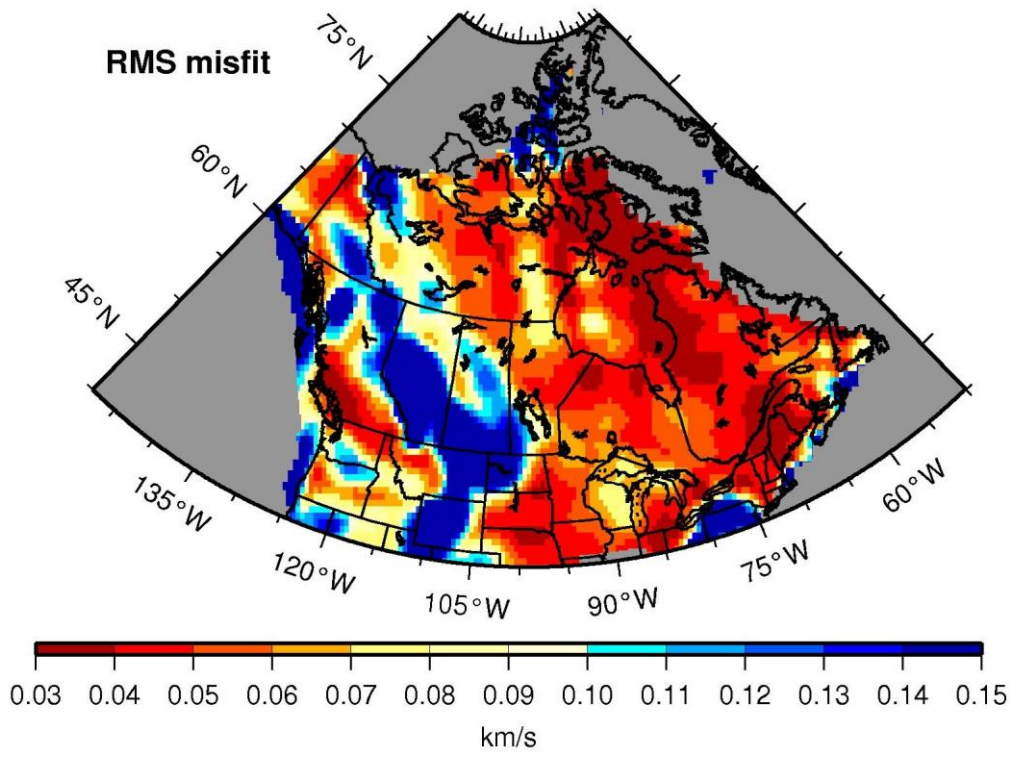
1110

1111 Figure 6c



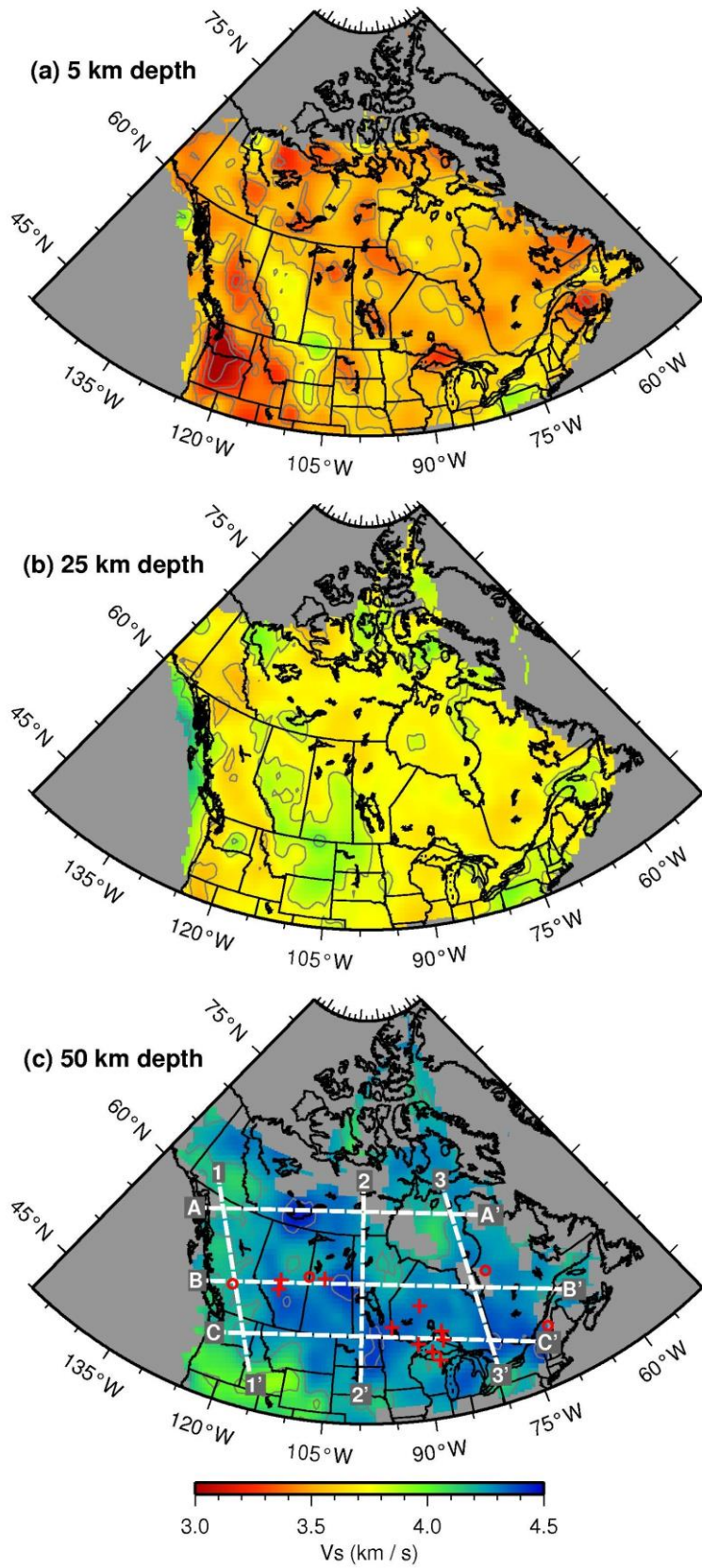
1112

1113 Figure 7



1114

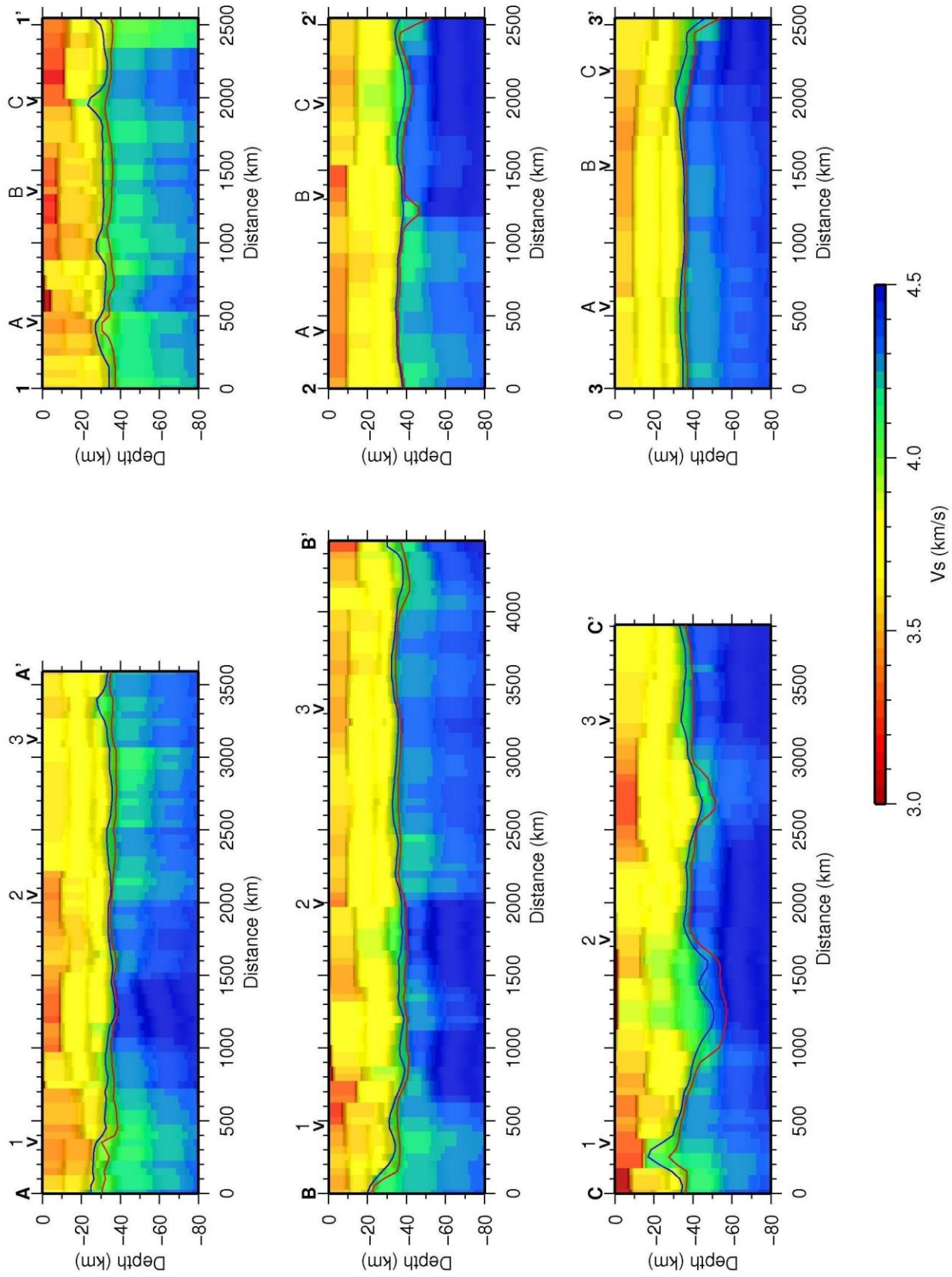
1115 Figure 8



1116

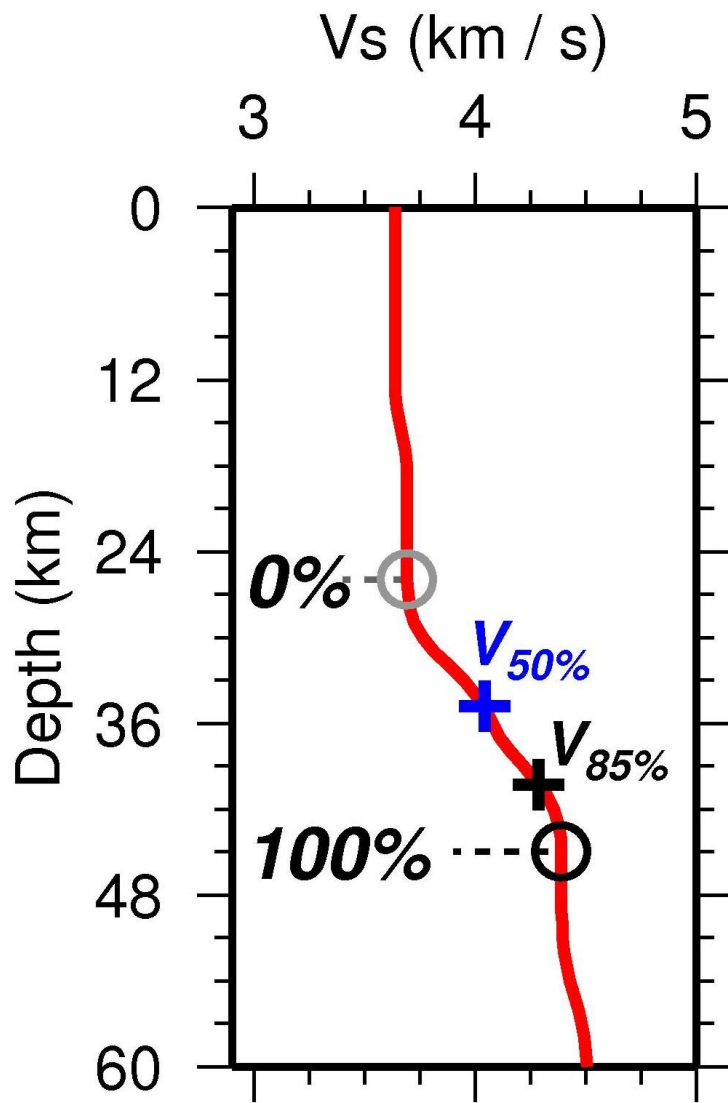
1117 Figure 9





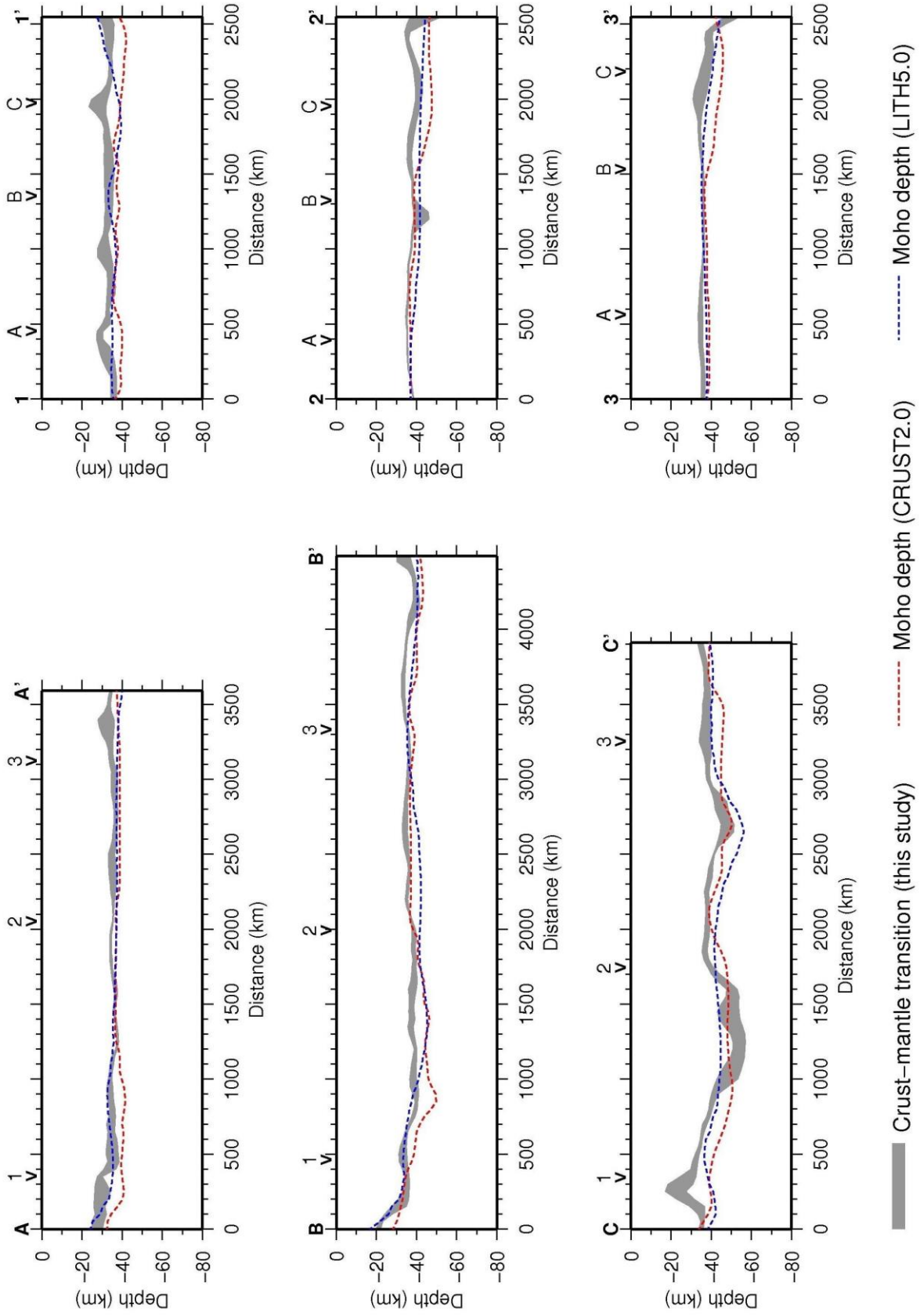
1118

1119 Figure 10



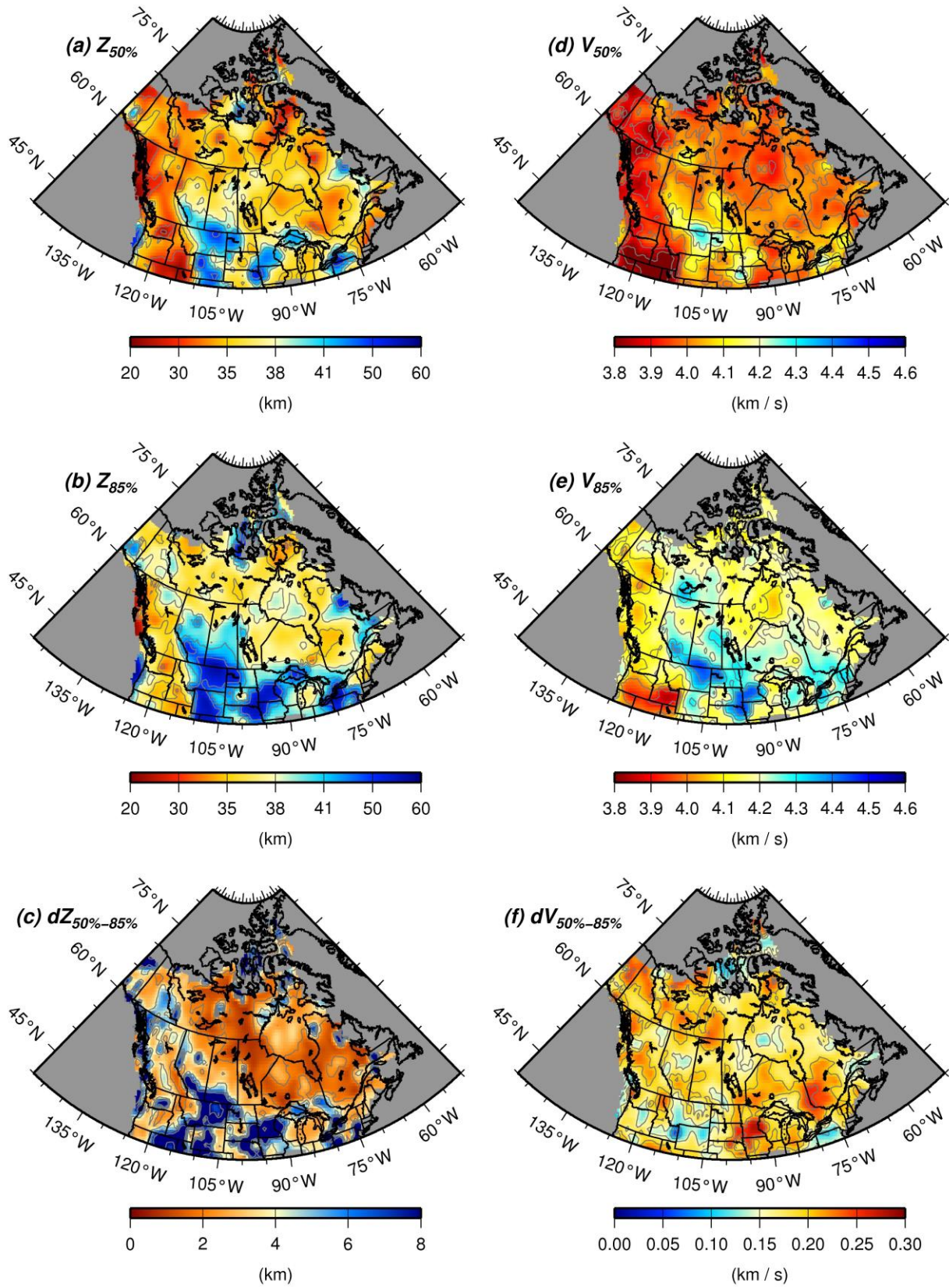
1120

1121 Figure 11



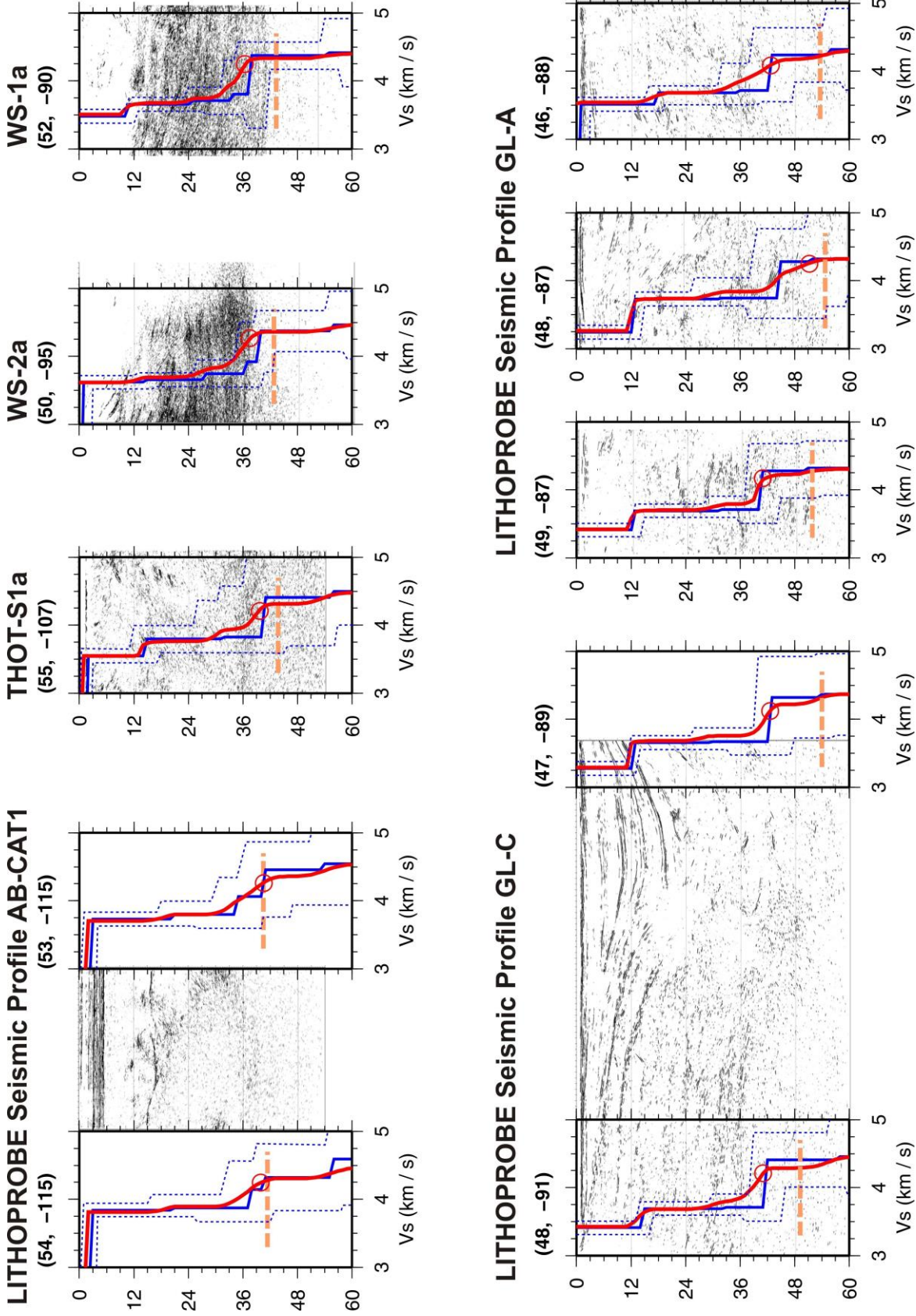
1122

1123 Figure 12



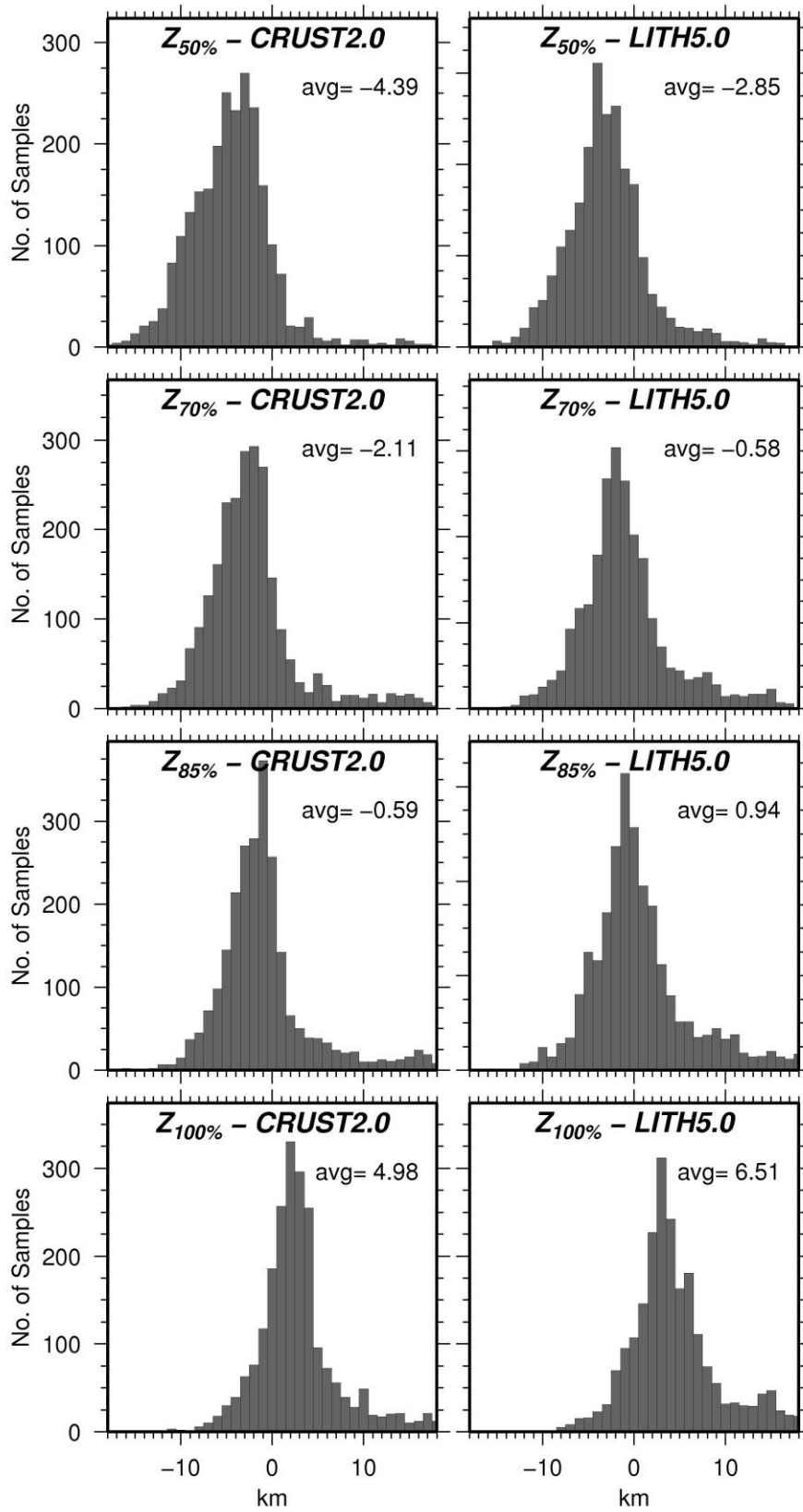
1124

1125 Figure 13



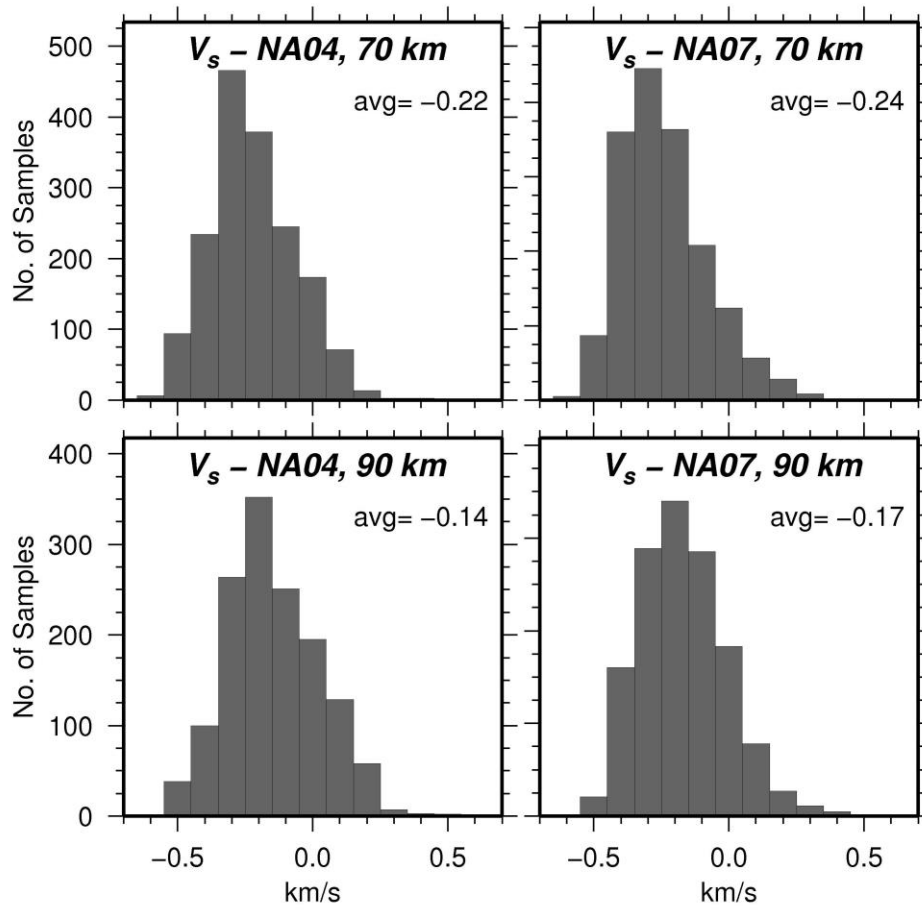
1126

1127 Figure 14



1128

1129 Figure 15



1130

1131 Figure 16